Jonathan Wolf[1] and Maureen D Long[1]

[1]Department of Earth and Planetary Sciences, Yale University

April 30, 2023

Lowermost mantle structure beneath the central Pacific Ocean: ultra-low velocity zones and seismic anisotropy

Jonathan Wolf[1], Maureen D. Long[1]

[1]Department of Earth and Planetary Sciences, Yale University, New Haven, CT, USA

Key Points:

- We identify and characterize a previously undetected ultra-low velocity zone beneath the central Pacific Ocean.
- We propose the existence of a thin and broad layer with low seismic velocities in our study region, just above the core-mantle boundary.
- Measurements of potentially co-located seismic anisotropy and ULVZ structure allow the inference of plausible dynamics in the deep mantle.

Corresponding author: Jonathan Wolf, `jonathan.wolf@yale.edu`

Abstract

Ultra-low velocity zones (ULVZs) and seismic anisotropy are both commonly detected in the lowermost mantle at the edges of the two antipodal large low velocity provinces (LLVPs). The preferential occurrences of both ULVZs and anisotropy at LLVP edges are potentially connected to deep mantle dynamics; however, the two phenomena are typically investigated separately. Here we use waveforms from three deep earthquakes to jointly investigate ULVZ structure and lowermost mantle anisotropy near an edge of the Pacific LLVP to the southeast of Hawaii. We model global wave propagation through candidate lowermost mantle structures using AxiSEM3D. Two structures that cause ULVZ-characteristic postcursors in our data are identified and are modeled as cylindrical ULVZs with radii of $\sim 1°$ and $\sim 3°$ and velocity reductions of $\sim 36\%$ and $\sim 20\%$. One of these features has not been detected before. The ULVZs are located to the south of Hawaii and are part of the previously detected complex low velocity structure at the base of the mantle in our study region. The waveforms also reveal that, to first order, the base of the mantle in our study region is a broad and thin region of modestly low velocities. Measurements of S_{diff} shear wave splitting reveal evidence for lowermost mantle anisotropy that is approximately co-located with ULVZ material. Our measurements of co-located anisotropy and ULVZ material suggest plausible geodynamic scenarios for flow in the deep mantle near the Pacific LLVP edge.

Plain Language Summary

Earthquakes cause different types of seismic waves that can be used to create an image of seismically fast and slow regions within Earth's interior. Two large-scale features with relatively low seismic velocities have been identified at the base of the mantle, one beneath Africa and one beneath the Pacific Ocean, known as large low velocity provinces (LLVPs). Small-scale, thin features with extremely low velocities, known as ultra-low velocity zones (ULVZs), have previously been detected just above the core-mantle boundary, often located at the edges of the LLVPs. In this study, we investigate a region of the deep mantle at the edge of the Pacific LLVP. We use recordings of earthquake waves that have sampled this region to map two distinct ULVZ regions at this boundary. We also investigate a property known as seismic anisotropy, the directional dependence of seismic wave speeds, which can be used to infer the direction of mantle flow.

We outline several potential mantle flow scenarios that are consistent with our data, helping to understand flow processes at the edges of LLVP structures in the deep mantle.

1 Introduction

The lower boundary layer of Earth's mantle, also called D$''$, has different seismic properties than the bulk of the lower mantle (e.g., Wookey et al., 2005b; Lay et al., 2006; Panning & Romanowicz, 2006; Kawai & Tsuchiya, 2009; Wenk & Romanowicz, 2017). These distinct properties are likely influenced by heat flux across the core-mantle boundary (CMB; e.g., Hernlund et al., 2005), possible chemical heterogeneity (e.g., Trampert et al., 2004), and by the details of lowermost mantle mineralogy (e.g., Murakami et al., 2004) and dynamics (e.g., Nowacki & Cottaar, 2021). The most prominent large-scale features in the lower mantle are the two antipodal large low velocity provinces (LLVPs) which show shear velocity reductions of up to $\sim$4% compared to the mantle average (e.g., Dziewonski et al., 2010; French & Romanowicz, 2014). While the precise nature of these large features is poorly understood (e.g., Davies et al., 2015; Koelemeijer et al., 2017; Davaille & Romanowicz, 2020), they are thought to have played a significant role in Earth's evolution (e.g., Burke et al., 2008; Steinberger et al., 2019; Wolf & Evans, 2022). For example, they have been suggested to significantly influence convective processes in the mantle (e.g., McNamara et al., 2010), plumes have been suggested to be preferentially found at their edges (e.g., Burke et al., 2008), and they may be important for our understanding of the supercontinent cycle (e.g., Wolf & Evans, 2022). It has been suggested that seismic anisotropy (that is, directionally dependent wave propagation) is particularly likely to occur in the lowermost mantle at the edges of LLVPs (e.g., Cottaar & Romanowicz, 2013; Deng et al., 2017; Reiss et al., 2019). This may reflect strong deformation, perhaps due to mantle flow impinging on their sides (e.g., McNamara et al., 2010; Li & Zhong, 2017), or to due the generation of mantle plumes (e.g., Burke et al., 2008). Additionally, thin ultra-low velocity zones (ULVZs) just above the CMB have been shown to cluster within or along the edges of LLVPs, although they are also present elsewhere (e.g., Yu & Garnero, 2018). The presence of both ULVZs and anisotropy at LLVP edges likely reveal information about deep mantle dynamics. However, these two phenomena are typically investigated separately.

While there is overwhelming evidence for the presence of ULVZs at the base of the mantle, no scientific consensus has been reached about their origin and composition. It has been suggested that iron from Earth's outer core may be responsible for their presence, either driven to the mantle by diffusion (e.g., Lesher et al., 2020) or via morphological instabilities (Otsuka & Karato, 2012). Alternatively, enrichment of iron in ferropericlase could explain the ultra-low velocities (e.g., Finkelstein et al., 2018; Lai et al., 2022). The presence of partial melt has also been suggested as an explanation for ULVZs (e.g., Lay et al., 2004; Yuan & Romanowicz, 2017; Ferrick & Korenaga, 2023), although it is imperfectly understood how melt pockets just above the CMB can stay stable over geological time scales (e.g., Hernlund & Jellinek, 2010; Dannberg et al., 2021). If ULVZs are made of solid material, they could be remnants of an early molten magma ocean (e.g., Labrosse et al., 2008; Pachhai et al., 2022). While it is likely that the present-day locations of ultra-low velocity zones are connected to patterns of mantle convection, this potential connection is still being actively investigated (e.g., McNamara et al., 2010; Li et al., 2017; Hernlund & Bonati, 2019). For example, mantle flow has been suggested to converge at LLVP edges (e.g., McNamara et al., 2010). If ULVZs can become entrained in mantle flow as suggested by some geodynamical models, they may therefore be driven towards the edges of LLVPs (e.g., McNamara et al., 2010; Li et al., 2017).

The presence of seismic anisotropy is a relatively direct indicator of mantle deformation (e.g., Long & Silver, 2009; Long & Becker, 2010; Wenk & Romanowicz, 2017). Measurements of lowermost mantle anisotropy have been explained by slab-driven flow (e.g., Nowacki et al., 2010; Asplet et al., 2020, 2023; Creasy et al., 2021; Wolf & Long, 2022), or upwelling flow at the bottom of mantle plumes (e.g., Ford et al., 2015; Wolf et al., 2019). It has also been demonstrated that lowermost mantle anisotropy can often be found close to the edges of the two LLVPs (e.g., Wang & Wen, 2004; Cottaar & Romanowicz, 2013; Lynner & Long, 2014; Deng et al., 2017; Reiss et al., 2019), indicating a likely change in mantle flow direction and/or a concentration of deformation, potentially connected to a rheological contrast. Because observations of both lowermost mantle anisotropy and ULVZs have been made at LLVP edges, their potential co-occurence may shed light on dynamic processes operating at the edges of LLVP structures.

A possible approach towards studying spatially coincident ULVZs and deep mantle seismic anisotropy is the analysis of S waves that are diffracted along the CMB (S_{diff} waves; Figure 1a). S_{diff} waves are often used for the detection and characterization of ULVZs (e.g., Cottaar & Romanowicz, 2012; Yuan & Romanowicz, 2017; Kim et al., 2020; Li et al., 2022) as well as seismic anisotropy (e.g., Cottaar & Romanowicz, 2013; Wolf

& Long, 2022; Wolf et al., 2023). For both approaches, the use of data from densely spaced seismic arrays has been proven to be advantageous (e.g., Li et al., 2022; Wolf et al., 2023). Array stacks can make visible signals that are arriving after the main S_{diff} phase, known as postcursors. The moveout of such postcursors as a function of azimuth can reveal the location and the properties of ULVZs (e.g., Cottaar & Romanowicz, 2012; Cottaar et al., 2022; Li et al., 2022). Additionally, the use of array data has been shown to be helpful when accounting for effects of upper mantle anisotropy (e.g., Wolf et al., 2023; Wolf et al., 2023). In addition to S_{diff} data, the use of S/ScS waves at long distances, shortly before they start to turn into S_{diff} (Figure 1a), has proven to be useful for analyzing ULVZs (e.g., Lai et al., 2022). In this study, we analyze such S/ScS waves together with S_{diff} for epicentral distances $> 95°$, and refer to the composite phase as S^* (following Lai et al. (2022)).

Here we investigate potentially co-located ULVZ structure and lowermost mantle anisotropy beneath the central Pacific Ocean, to the southeast of Hawaii, using S^* phases. We target a region at the eastern edge of the Pacific LLVP that has previously been suggested to host ULVZ material. Based on the analysis and modeling of S^* phases, we suggest the presence of a widespread, thin low-velocity layer just above the CMB in our study region, possibly associated with the base of the Pacific LLVP itself. We also find evidence for two distinct ULVZs, one of which has not been detected previously. We identify evidence for lowermost mantle anisotropy for a portion of the S_{diff} raypaths that sample across the LLVP edge; this anisotropy is spatially approximately co-incident with ULVZ structure. Measurements of splitting parameters due to lowermost mantle anisotropy allow us to analyze the plausibility of different mantle flow scenarios close to ULVZs and the LLVP edge.

2 Study region

Our study region is to the southeast of Hawaii, at the edge of the Pacific LLVP. Figure 1c shows the raypath coverage and the locations of previously detected ULVZ structure in this region (Yu & Garnero, 2018; Sun et al., 2019; Lai et al., 2022), in addition to the low velocity features mapped by Jenkins et al. (2021). Early studies using core-reflected P waves suggested a ∼10 km thick basal layer with velocity reductions of approximately 10 % in our study region (e.g., Mori & Helmberger, 1995; Revenaugh & Meyer, 1997). Later studies used ScS waves to map more detailed structure (e.g., Avants et al., 2006; Lay et al., 2006; Hutko et al., 2009), arguing for more dramatic S- than P-wave velocity reductions. Recently, Jenkins et al. (2021) provided a more comprehensive picture of ULVZ structure throughout the region, suggesting either decreasing seismic velocities and/or an increasing ULVZ thickness moving towards the LLVP edge from its center. Other recent studies identifying individual ULVZs in our study region are from Sun et al. (2019) and Lai et al. (2022). Lai et al. (2022) used data from event 1 (Figure 1c) that we also analyze in our study, although they focused on longer periods (5–80 s).

The presence of lowermost mantle anisotropy in our study region has been previously suggested by some early studies that investigated differential $\mathrm{SH_{diff}}$ -$\mathrm{SV_{diff}}$ travel times (e.g., Vinnik et al., 1995, 1998; Ritsema et al., 1998). Another study used S and ScS waves to map radial anisotropy in our study region, finding $V_{SV} > V_{SH}$ 200-400 km above the CMB (Kawai & Geller, 2010). However, no previous study has directly measured fast polarization directions of deep mantle anisotropy in our region of interest. Here we take advantage of newly developed strategies for measuring the splitting parameters of $\mathrm{S_{diff}}$ phases (Wolf et al., 2023) to place tighter constraints on the geometry of deep mantle anisotropy in the region.

3 Data and Methods

3.1 Event selection

In this study, we analyze recordings of deep and intermediate events that occurred in (or close to) the Tonga subduction zone, which are in the right distance range for the study of our target region using the dense USArray (IRIS Transportable Array, 2003) as well as other nearby stations. USArray consisted of hundreds of broadband seismometers that were moved from west to east across the contiguous United States between 2007 and 2013. First, we create a list of 27 candidate events (Supplementary Table S1) that have a high likelihood of providing high-quality data, based on moment magnitude (preferably around ∼6.5) and depth (> 100 km). We prefer deep events because they are unlikely to be strongly influenced by source-side anisotropy; furthermore, postcursors for our ULVZ analysis are most likely to be visible for large events with simple source-time functions, as is often the case with deep events. After an initial visual quality control step, we display data for each event as a function of distance and/or azimuth, stacked in 0.5° to 1.5° azimuth or distance bins (dependent on number of data), similar to Figures 2 and 3. While the number of traces contributing to each bin varies, the average number of traces is always larger than 25. For our ULVZ analysis, we look for generally high-quality transverse component (SH) data that show typical S* postcursors as a function of azimuth on the transverse components, indicating the presence of ULVZs (e.g., Cottaar & Romanowicz, 2012). The data from event 1 (Figure 1c) show an outstandingly clear main S* signal with signal-to-noise ratios (SNRs) that are > 10 across most stations compared to pre-event noise, and unambiguous postcursors (Figure 2a). While for many events the data are too noisy to reliably characterize S* postcursors, we do identify several additional events with clear S* signals that show similar postcursors, but less clearly (Supplementary Figures S1, S2 and S3). Because of its exceptional signal quality, we focus on data from event 1 for our ULVZ analysis.

For the analysis of deep mantle seismic anisotropy, we follow the proposed S_{diff} splitting strategy from Wolf et al. (2023), which relies on the comparison of splitting from SKS and S_{diff} phases (Figure 1a) to identify deep mantle anisotropy. The S_{diff} splitting strategy includes two steps to ensure that the measured S_{diff} splitting can in fact be attributed to seismic anisotropy in the lowermost mantle or on the receiver side. The first step is to show that the S_{diff} waves under study do not sample strong upper mantle anisotropy on the source side, leading to splitting intensities (Equation (4), discussed in detail below) larger than 1. To ensure this, we search for events with focal depths > 300 km. While S_{diff} from such events may realistically sample some source-side anisotropy, the contribution is unlikely to be strong (e.g., Foley & Long, 2011; Lynner & Long, 2015). Second, it must be guaranteed that S_{diff} for the event would be almost perfectly SH-polarized in absence of seismic anisotropy because otherwise differential SH_{diff}-SV_{diff} travel times may be accumulated in isotropic structure, potentially resembling splitting (Komatitsch et al., 2010; Borgeaud et al., 2016; Parisi et al., 2018). Upon diffraction, when S and ScS combine to a single phase, their radial amplitudes are approximately opposite, which is why usually SV_{diff} energy is lost in the process (Wolf et al., 2023). Therefore, it is likely that S_{diff} is substantially SH-polarized. However, how much SV_{diff} energy survives does not only depend on the focal mechanism but also on the lowermost mantle velocity structure, which is why it is necessary to test this via global wavefield simulations (Wolf et al., 2023) using the best moment tensor estimate (Ekström et al., 2012). For the S_{diff} splitting analysis, the main factor why events are discarded is not the SNR (as for the

ULVZ analysis) but the requirement for S_{diff} to be almost perfectly SH-polarized in the absence of seismic anisotropy along the raypath.

The only event that fulfills these criteria and exhibits high-quality S_{diff} signals with SNRs$>$ 3 across most seismograms is event 2 (Figure 1d, Figure 3). However, due to its strong SH initial source polarization, SKS phases for this event are noisy in the azimuth range of interest; therefore, we also analyze SKS for a third event (event 3), which exhbits SNRs > 4 for most SKS waves, to better resolve receiver-side upper mantle anisotropy. Event 3 is chosen because it occurred at a similar location and with similar timing (less than a month later) as event 2. Therefore, events 2 and 3 have been recorded at a very similar selection of Transportable Array stations. The similar timing of events 2 and 3 allows us to account for the potential effects of upper mantle anisotropy, discussed further in Section 5.3. We use all available stations (mostly from USArray) located at an appropriate epicentral distance and azimuth that were installed at the time that events 2 and 3 occurred and only discard obviously corrupted data.

3.2 Global wavefield simulations

For the analysis of ULVZ postcursors of S^* phases from event 1, we conduct 3D waveform modeling with AxiSEM3D (Leng et al., 2016, 2019), computing simulations down to periods of $\sim$4 s. Our general approach to model setup and parameterization is similar to our approach in previous work for simulations that include lowermost mantle anisotropy and ULVZ structure (e.g., Wolf et al., 2022a; Wolf et al., 2023). As in this previous work, our background model is always isotropic PREM (Dziewonski & Anderson, 1981), and for certain simulations we replace the PREM mantle with the 3D tomographic model GyPSuM (Simmons et al., 2010). For all our simulations we include Earth's ellipticity and (PREM) attenuation. We use focal mechanisms as reported by the Global CMT Catalog (Ekström et al., 2012). However, in this work we need to be particularly aware of computational efficiency; AxiSEM3D expands the wavefield along the azimuthal direction using a Fourier basis, giving the user the option to choose the maximum Fourier expansion order N_u (Leng et al., 2016). For models that include complex, small-scale structures, a high Fourier expansion order is required to adequately represent the wavefield. In our simulations, we first select lower N_u values (< 300) to make an educated guess about likely ULVZ positions and properties. Then, we perform more expensive simulations for higher N_u (up to 1000), while making full use of the incorporated wavefield learning tool in AxiSEM3D (Leng et al., 2019) for similar simulations. We always ensure that the selected N_u values are large enough by checking that all N_u in the wavefield output are lower than the maximum constant N_u used in the learning simulation, or by benchmarking each type of simulations against higher N_u values. We also ensure that the mesh is able to accurately capture the structures we incorporate. Using our maximum available allocation on the Grace cluster at Yale University (1000 CPUs in parallel; more only in rare exceptions), we are able to reliably perform fully 3D global wavefield simulations down to periods 5 s to investigate the S* postcursors for event 1 (Figure 2a). To investigate the distance-dependent behavior of S and S_{diff} waves (Figure 2d), which can be observed in a period band between 4 s and 10 s, we have to rely on (mostly) axisymmetric input models (using PREM with a global low velocity layer; see Section 5.1). These axisymmetric simulations are > 100 times faster to run than simulations with 3D ULVZs. Only for a small subset of simulations can we compute synthetic waveforms down to 4 s incorporating 3D velocity structure.

3.3 Shear-wave splitting measurements

The analysis of shear-wave splitting is largely independent of our analysis of possible ULVZ structure. For the measurement of deep mantle anisotropy we analyze shear wave splitting of events 2 and 3, while event 1 is used to infer ULVZ structure. A shear wave that travels through an anisotropic medium splits into two quasi shear waves, one slow and one fast. If the incoming harmonic wave is SV-polarized (e.g., SKS), ω is the angular frequency and t is time, assuming that $\omega t \ << \ 1$, the radial component $R(t)$ can be written

$$R(t) \simeq \cos \omega t \tag{1}$$

(Vinnik et al., 1989; Silver & Chan, 1991). When the wave has traveled through an anisotropic medium, the transverse component can then be expressed as

$$T(t) \simeq -0.5\omega\delta t \sin 2(\alpha - \phi) \sin \omega t = 0.5\omega\delta t \sin 2(\alpha - \phi) R'(t) \ , \tag{2}$$

where $R'(t)$ is the radial component time derivative, δt is the time lag between the fast and slow traveling quasi S-wave, ϕ is the polarization direction of the fast traveling wave, and α the initial polarization direction of the incoming wave (equivalent to the backazimuthal direction). The fast polarization direction ϕ is measured clockwise from the north, while ϕ' denotes the same quantity measured clockwise from the backazimuthal direction (Nowacki et al., 2010). The schematic illustration of ϕ' in Figure 1b shows that $\phi' \approx 0°$ corresponds to vertical and $\phi' \approx 90°$ to horizontal fast polarization directions of lowermost mantle anisotropy. A related quantity, called splitting intensity (Chevrot, 2000), related to the splitting delay time and thus the strength of splitting, is defined as

$$SI_{SV} = -2\frac{T(t)R'(t)}{|R'(t)|^2} \approx \delta t \sin(2(\alpha - \phi)) \tag{3}$$

for SKS. For S_{diff} waves that can be assumed to be initially SH-polarized (as we use in our study), we calculate the splitting intensity following Wolf et al. (2023), using the formula

$$SI_{SH} = -2\frac{R(t)T'(t)}{|T'(t)|^2}\ , \tag{4}$$

where $T'(t)$ is the transverse component time derivative.

To estimate the splitting parameters (ϕ, δt; SI) we use SplitRacer (Reiss & Rümpker, 2017), a graphical user interface implemented into MATLAB. SplitRacer calculates splitting parameters for multiple time windows (we always choose 50) using the transverse component minimization technique (Silver & Chan, 1991). The corresponding 95% confidence intervals are estimated using the corrected algorithm of Walsh et al. (2013). We use a modified version of SplitRacer that calculates ϕ' instead of ϕ and measures Sdiff splitting according to Equation (4). We also switch the radial and transverse component to measure S_{diff} splitting. We call the fast polarization direction obtained this way ϕ'', which equals $90° - \phi'$ (Wolf et al., 2023).

4 Results: Waveform characteristics

The data from events 1 and 2, which we use to constrain ULVZ structure and anisotropy, respectively, are shown in Figures 2 and 3. The data from event 1 exhibit several features that are not reproduced in synthetics for simple models, either for PREM (Dziewonski & Anderson, 1981, Figure 2g-i) nor for the 3D tomographic model GyPSuM (Simmons et al., 2010, Figure 2d-f). These data characteristics are as follows (Figure 2):

1. A prominent S^* postcursor, visible directly after the S^* phase and modeled as being due to an ULVZ by Lai et al. (2022), is (marked with a pink box in Figure 2a).

As this waveform feature has been modeled and explained before, we do not focus on it in our analysis. To model this postcursor, we would have to add one additional ULVZ to our simulations; this would have little to no influence of the other modeled postcursors and would be unlikely to add more insights beyond the results of Lai et al. (2022).

2. Two postcursors with hyperbolic moveout are marked in blue and green in Figure 2a. Because these postcursors may indicate previously undetected ULVZ structures, we focus our modeling on these features. The ULVZ will be located approximately at the azimuth at which the postcursor arrives closest in time after the main Sdiff arrival. This azimuth differs greatly for both hyperbolic postcursors, such that they cannot be explained by a single ultra-low velocity structure. Instead, multiple ULVZ regions are needed to produce both features.
3. When filtering the data with a center frequency of 7 s, the real data (Figure 2c) look very different from the PREM/GyPSuM synthetic data as a function of distance (Figure 2f,i), especially for an epicentral distance $> 95°$, shortly before S starts to turn into S_{diff}. The most prominent feature of the waveforms is that for S^* the second downswing (orange shading in Figure 2c) is the larger than the first, opposite to what is predicted from the synthetics (Figure 2f,g).
4. The radial component of the main S_{diff} arrival becomes larger with more northerly (that is, smaller) azimuths (blue shading in Figure 2b). While some of this energy can likely be explained as being due to the initial source polarization (Figure 2e,h), we speculate that it could also partially be due to deep mantle anisotropy (and will test this possibility in detail using data from event 2).

For the analysis of seismic anisotropy we focus on longer periods (8-25 s) than for our ULVZ investigation. At these periods, the transverse components for event 2 (Figure 3a) do not show postcursors, although faint postcursors can be detected for this event when the data are bandpass-filtered retaining periods between 6 and 20 s (Supplementary Figure S1). Event 2 was chosen because S_{diff} waves for this event can be expected to be almost perfectly SH-polarized, especially at more northerly azimuths (Figure 3c,d). However, radial components from event 2 show clear S_{diff} arrivals for azimuths between 45° to 52°, indicating splitting along the raypath, possibly due to the presence of lowermost mantle anisotropy.

5 Results: Forward modeling

5.1 Thin, broad low velocity layer

The distance-dependent behavior of the S and S_{diff} data from event 1 is presented in Figure 2c and Figure 4a. We focus on the main features, which we retrieve by stacking the data in 1.5° wide distance bins (Figure 4a). The data characteristics that we strive to explain are: 1) the absence of substantial energy after the main S arrival for distances between ∼87°−95°, and 2) the presence of a large second downswing of S^* for distances $> 95°$, potentially indicating the arrival of postcursor energy that is interfering with the main S^* arrival. Neither of these features is predicted by the simple synthetics, either for isotropic PREM or for the GyPSuM mantle model (Figure 4).

As previous observations suggest (Section 2), there may be lower than average seismic velocities just above the CMB in our study region. We therefore generate synthetics for a geographically widespread layer (modeled for simplicity as a global layer, which allows us to carry out axisymmetric simulations) with lower than average seismic velocities. We simulate wave propagation for layer thicknesses between 5 km and 50 km, and for velocity reductions between 2 % and 60 %. While only velocity reductions in a relatively tight interval can explain the observations for a given thickness, there is a clear tradeoff between layer thickness and velocity reduction that makes it difficult to precisely constrain thickness and velocity reduction together (as we will discuss further in Section 6.1). In order to tightly constrain the best-fitting parameters, we adaptively sample our parameter space and run simulations in 5 km thickness increments and at most 5 km velocity reduction increments for a narrow parameter interval. Our preferred model to explain these data features is a widespread layer with a thickness of 5 km and a shear-wave velocity reduction of 14 % compared to PREM. The corresponding PREM and PREM+GyPSuM synthetics are shown in Figure 4d and e. It is visually apparent that this low velocity layer is able to explain the aforementioned main data features. To more objectively assess the similarity of real and synthetic data, we cross-correlate the real and synthetic seismograms, for 55 s long time window around the predicted arrival time, all bandpass-filtered retaining periods between 4 and 10 s. The average cross-correlation coefficients increase from 0.84 to 0.90 for PREM and from 0.83 to 0.87 for GyPSuM when incorporating this widespread low velocity feature.

5.2 Two regions causing S^* postcursors

The postcursors that can be observed as a function of azimuth in the S* data from event 1 (Figure 2a) can be explained by the presence of two ULVZs, one of which located in the north and the other located in the south of our study region. The northern ULVZ identified by our modeling is co-located with previously observed ULVZ structure, while the southern ULVZ has not been mapped before (discussed further in Section 5.4). It is likely that these two ULVZ regions do not represent distinct features; rather, they are likely connected to the highly variable, low-velocity structure that has been identified previously throughout our study region (e.g., Avants et al., 2006; Jenkins et al., 2021). For our modeling we assume cylindrical ULVZ regions with a thickness of 10 km, which is within the range that has been previously suggested for our study region (e.g., Avants et al., 2006; Jenkins et al., 2021). We simulate velocity reductions from 10 % to 60 % and base area radii between 1° and 7°. The best fitting combination of size, velocity reduction and location for the two ULVZs are as follows:

- Northern ULVZ: Shear-wave velocity reduction 20 %; radius 3°; centered at (150°W, 8°N).
- Southern ULVZ: Shear-wave velocity reduction 36 %; radius 1°; centered at (139°W, 0.5°N).

The real data and the synthetic data, modeled for the aforementioned dimensions and velocity reduction of the ULVZs, are shown in Figure 5. Our model successfully captures the general features of both postcursors. However, the PREM synthetics (Figure 5b) match the real data (Figure 5a) better than the PREM+GyPSuM synthetics (Figure 5c) for the postcursor from the northern ULVZ. The reason for this is that the 'shoulder' of the S* pulse is longer in time for the PREM synthetics, which approximates the real data more accurately. Changing the structure for the northern ULVZ would not change this fact, and would therefore not improve the fit for the PREM+GyPSuM background model. While our modeling has identified best-fitting ULVZ parameters for each region, there are of course tradeoffs between the ULVZ dimensions and the velocity reductions; In lieu of providing quantitative confidence intervals, which would be too computationally expensive to obtain using our forward modeling approach, we provide a detailed discussion of tradeoffs between model parameters in Section 6.1.

5.3 Lowermost mantle anisotropy

As demonstrated in Figure 3, S_{diff} waves from event 2 show evidence for shear wave splitting, and thus the presence of seismic anisotropy, along their raypaths. In order to determine the location of the anisotropic structure along the raypath, and in particular to distinguish between anisotropy in the upper vs. lowermost mantle, we stack SKS waves from event 2 as a function of azimuth in 1° azimuth bins (Figure 6a,b). SKS splitting is generally thought to mainly reflect upper mantle anisotropy because upper mantle splitting delay times are generally larger than delay times in the lower mantle (e.g., Panning & Romanowicz, 2006). In contrast to SKS, S_{diff} has a long horizontal raypath through the deep mantle along which it can accumulate splitting, which is why S_{diff} is sometimes strongly influenced by lowermost mantle anisotropy. If splitting of S_{diff} occurs in the upper mantle beneath the seismic stations, SKS will be split too; therefore, differences in the splitting behavior of Sdiff vs. SKS would indicate a contribution to S_{diff} splitting from the lowermost mantle (Wolf et al., 2023). While there is no evidence for coherent energy split to the SKS transverse component, it is not entirely clear whether the apparent absence of splitting is robust considering the noise level (Figure 6b). It has been shown that a lack of visible splitting, even in the presence of anisotropy, can be caused by high noise levels (e.g., Wolf et al., 2023). In order to further test this possibility, we additionally analyze the SKS signals from event 3 (Figure 6b). Event 3 is chosen because it occurred at a similar location and with similar timing (less than a month later) as event 2 and was therefore recorded at almost the same set of Transportable Array stations. We stack the data in the same way as for event 2, only using stations that were also used for event 2. The stacks for event 3 show a very low level of noise and only negligible coherent transverse component energy. This means that upper mantle anisotropy is likely laterally heterogeneous in all azimuth bins, averaging to ∼null splitting in the corresponding stack (Wolf et al., 2023). Because upper mantle anisotropy has only slight effects on the SKS stacks (Figure 6), the anisotropic signal for S_{diff} (Figure 3) can be largely attributed to the presence of lowermost mantle anisotropy, and potentially unreliable explicit upper mantle anisotropy corrections (Wolf et al., 2022b) can be avoided.

Next, we measure the splitting intensity for each azimuth bin for S_{diff} from event 2, as well as for SKS from events 2 and 3 (Figure 7a). As expected from the waveform plots, SKS splitting measurements for events 2 and 3 are very similar and almost null for the whole azimuth range. In contrast, S_{diff} is clearly split for the azimuths between

45° and 49°. We suspect that the apparent splitting measured from the SKS stacks of event 2 in the azimuth range 49° to 54° is mainly due to noise, since the visible transverse energy in this azimuth range is not higher than the noise level (Figure 6a). We assume that the higher SNR data from event 3 produces more reliable SKS splitting measurements in this region; again, these show null results, and thus when compared to S_{diff} splitting for event 2 argue for the presence of splitting due to lowermost mantle seismic anisotropy in this azimuth range too. While we view this possiblity as likely, we cannot make a definitive judgment about the presence of lowermost mantle anisotropy for azimuths between 49° and 54° because of the potential SKS splitting seen for event 2. For azimuths $> 54°$, we do not find evidence for the presence of lowermost mantle anisotropy. This implies that lowermost mantle anisotropy is likely absent; however, it possible that seismic anisotropy is sampled by S_{diff} from a null direction, and cannot therefore be detected using data from a single azimuth.

In order to constrain the geometry of anisotropy in the lowermost mantle, we further analyze the S_{diff} data over the azimuth range for which we have demonstrated the presence of lowermost mantle anisotropy (45° to 49°; Figure 7a). The radial components show a coherent signal in this azimuth range (Figure 3). Therefore, we decide to stack the data for the whole azimuth range to minimize noise (Figure 7b) and then measure the corresponding (laterally averaged) splitting parameters (Figure 7c). The corresponding splitting parameters are robust with $\delta t \approx 0.7\,\text{s}$ and $\phi' \approx 20°$, implying anisotropy in $V_{SV} > V_{SH}$ geometry (Figure 7c).

5.4 Synopsis: ULVZs and seismic anisotropy at the LLVP edge

We display the overall results from our ULVZ and anisotropy analysis in Figure 8. Several aspects of the inferred geometry are notable. The northern ULVZ is located close to the region where Jenkins et al. (2021) also reported a patch of particularly low seismic velocities, although there is an uncertainty associated with the location of our identified ULVZ (see dashed lines in Figure 8; this uncertainty is discussed further in Section 6.1). Therefore, it is likely that we are mapping the same feature as Jenkins et al. (2021) with similar dimensions but using a different seismic phase (S_{diff}, as opposed to ScS). The southern ULVZ, which to our knowledge has not been detected before, is likely located either just at the edge of the Pacific LLVP or just inside of it. ULVZ structure is most easily visible in S_{diff} data if characteristic postcursors can be observed, and previously detected ULVZ structure has mostly been mapped using different seismic phases with different sensitivity to lowermost mantle structure. Therefore, we do not consider the fact that we do not resolve all the structure mapped by Jenkins et al. (2021) as a contradiction to this previous work. However, we do not show all the features that Jenkins et al. (2021) show, probably due to the different sensitivities with our method.

Our findings that a 5 km thin, continuous layer of low velocities can explain some patterns visible in our data and that other patterns indicate ∼10 km thick ultra-low velocity features at the base of the mantle, do not contradict each other. For each of the analyses, we analyze different frequency ranges, bandpass-filtering our data between 4−10 s and 5−20 s respectively. While the hyperbolic postcursors indicating two distinct ULVZs are also visible in the frequency range between 4−10 s, they are visible less clearly. Similarly, the data features that we model to suggest a continuous layer of low velocities at the base of the mantle are also visible between $5-20$ s, but are much less pronounced. A likely explanation for our findings is that there is a relatively continuous layer of low velocities just above the CMB in our study region, whose thickness and velocity reduction varies somewhat laterally. The two regions in which the thickness of this layer is the largest, or the velocity is the lowest, cause the two postcursors that we model in our data as two ULVZs. Therefore, distinguishing them as separate structures from the widespread low velocity layer is somewhat arbitrary, but agrees with the way that the term ULVZ has previously been used in the literature.

The two ULVZs found in this study are most likely not sampled by data from event 2 that we used to detect deep mantle anisotropy, although the northern ULVZ might be just at the edge of the anisotropic structure (Figure 8). However, the lowermost mantle anisotropy is strong for data that sample ULVZ structure mapped by Jenkins et al. (2021) and compiled by Yu and Garnero (2018) along much of their raypath (Figure 8). For raypaths in our study that do not sample any previously detected ULVZ structure, there is no evidence for lowermost mantle anisotropy.

6 Discussion

6.1 Tradeoffs among model parameters

Our data suggest the presence of a broad and thin low velocity layer (velocities of −14 %) at the base of the mantle in our study region, but there are likely tradeoffs between the inferred thickness and velocity reduction. We have shown that the distance-dependent S^* behavior, indicative of such a layer, cannot be explained by a 3D tomographic model (Figure 2c), which includes modest velocity reductions (of a few percent) in LLVP regions. In order to understand the tradeoffs between model parameters, we investigated a series of models and found that models with a 10km or 20 km thick layer and velocity reductions of 7.5 % and 4 % gives similar results to our preferred 5km thick ULVZ layer. However, for these alternative models, the moveout of the S^* phase as a function of distance looks dissimilar to the real data (Supplementary Figure S4), leading to an average cross-correlation coefficient that is minimally lower (0.01-0.02). Additionally, a characteristic 'double pulse' that can be observed in the real data can be explained only by the presence of a thin and broad low-velocity layer (Supplementary Figure S5). However, the layer could possibly be thinner than 5 km with a more drastic velocity reduction and still explain all the aforementioned features. A thinner layer would, however, be hard to resolve, given the sensitivity of S_{diff} waves to structure just above the CMB at the analyzed frequencies (Li et al., 2022). The suggestion that such a low velocity layer might exist globally just above the CMB, but that it is often invisible to seismic data, has been made before, most recently by Russell et al. (2022). In our case, event 1 provides exceptionally clear signals, allowing such a very thin low-velocity layer to be resolved. The quality of the other events analyzed for this study would not have been sufficient to find such a feature. As the general data characteristics that indicate the presence of this layer are present for the whole azimuth range (Supplementary Figure S5), the data do not constrain its lateral boundaries. Because the location where S turns into S_{diff} is well within the LLVP boundaries, we cannot resolve with certainty whether this thin low-velocity layer extends beyond the LLVP border.

Our ULVZ modelling in this work has relied on the assumption that the ULVZ is cylindrical with a thickness of 10 km. As is typical in ULVZ detection studies, neither the detailed shape nor the exact thickness of the ULVZ can be fully resolved with our data: ULVZ shape is unclear because we do not sample the ULVZs from multiple azimuths, while the ULVZ thickness will trade off completely with the velocity reduction needed to explain the postcursors. The free parameters that we are changing in our modelling are radius, velocity reduction and location of the ULVZ; however, the effects of all three parameters on the postcursors are not completely independent. We can resolve within one or two degrees the location of the ULVZ center in the direction perpendicular to the raypath, as this corresponds to the azimuths at which the precursors arrive with the smallest delay time behind the main S_{diff} arrival. The location of the ULVZ in the direction along the S^* raypaths is somewhat more difficult to resolve (as indicated by red dashed lines in Figure 8). We infer that the ULVZs are likely located where S turns into S_{diff} or only shortly behind it, just inside the Pacific LLVP (Figure 8). This is because S phases for distances $> 95°$, in addition to Sdiff phases, show the characteristic postcursors indicating the presence of ULVZ material.

As discussed in Section 5.4, for raypaths that sample the eastern portion of our study region, we do not find evidence for the presence of lowermost mantle anisotropy (Figure 7a). The inferred deep mantle anisotropy is spatially coincident with previously mapped ULVZ structure (Figure 8). Moreover, while our stacking approach is excellent to suppress noise in order to retrieve well-constrained spatially integrated time delay and fast polarization direction measurements (for azimuths 45° to 49°), our use of stacking means that we are unable to resolve smaller scale changes of these splitting parameters.

6.2 Geodynamic implications

As mentioned above, our data do not allow us to precisely constrain where along the raypath through the lowermost mantle S_{diff} waves sample lowermost mantle anisotropy. Seismic anisotropy could be located within the ULVZ structure (Figure 9a) or either inside (b) or outside (c) the edge of the ULVZ (or any combination of these). These three possibilities are not distinguishable with our data. Despite these limitations of our data, we can use these inferences to distinguish between geodynamic scenarios that are incompatible with our observations and those that are plausible.

Several different scenarios have been suggested to explain the presence of seismic anisotropy in D″, including the lattice-preferred orientation (LPO) of lowermost mantle minerals such as post-perovskite, bridgmanite, and/or ferropericlase (e.g., Wookey et al., 2005b; Nowacki et al., 2011; Creasy et al., 2020) or the shape-preferred orientation (SPO) of materials with contrasting elastic properties (e.g., Kendall & Silver, 1998). Furthermore, several possible explanations for the presence of ULVZ material, including a liquid iron infiltrating the mantle from the core (Otsuka & Karato, 2012) and the presence of iron-rich ferropericlase (Finkelstein et al., 2018; Lai et al., 2022), have implications for anisotropic structure. If seismic anisotropy is caused by liquid iron that moved upwards from the outer core (e.g., Otsuka & Karato, 2012; Lesher et al., 2020), forming ULVZs and creating shape-preferred orientation (SPO), the material would likely be in a horizontally layered configuration parallel to the CMB. In this case $V_{SH} > V_{SV}$ would be expected, which is the opposite of what we observe. In fact, we observe $V_{SV} > V_{SH}$, which is incompatible with such a horizontal layering. Our measurements of $V_{SV} > V_{SH}$ agree with the anisotropy mapped by Kawai and Geller (2010) 200 to 400 km above the CMB in our study region.

A plausible scenario is that the inferred lowermost mantle anisotropy can be explained by lattice-preferred orientation (LPO) in the lowermost mantle within or outside the LLVP (Figure 9a). In theory, measurements of deep mantle anisotropy splitting parameters can be used to constrain plausible flow scenarios if the anisotropy is due to LPO (e.g., Ford et al., 2015; Creasy et al., 2021; Wolf & Long, 2022; Pisconti et al., 2023). For such an exercise, however, it would be necessary to measure splitting parameters for multiple backazimuths and/or multiple phases (Creasy et al., 2019). Unfortunately, for our study region, we cannot identify high-quality S_{diff} phases sampling the lowermost mantle from different backazimuths. Neither is our study region suitable to infer deep mantle anisotropy using other commonly used phases like SK(K)S or ScS, due to the distribution of sources and receivers around the Pacific. Therefore, while our measurements are generally compatible with seismic anisotropy due to LPO, we do not have enough information to constrain plausible directions of deformation and flow in this case.

If lowermost mantle anisotropy is caused by SPO of partial melt or solid material with very low seismic velocities, located outside of ULVZ structure, our observations are compatible with the entrainment of this material by upwelling flow (leading to $V_{SV} > V_{SH}$), perhaps at the edge of the LLVP. Such a material could, for example, originate from ULVZs and would have to be stretched in the vertical direction. This scenario would be compatible with the observation that mantle plumes are preferentially located at the edges of the two LLVPs (e.g., Torsvik et al., 2014). In fact, the lowermost mantle anisotropy is located approximately where Hassan et al. (2016) suggest the root of the plume giving rise to the Hawaiian-Emperor seamount chain is present. However, the findings from Hassan et al. (2016) are not obviously consistent with global tomography models (e.g., Ritsema et al., 2011; French & Romanowicz, 2014; Hosseini et al., 2019), which rather suggest a vertically extending plume structure directly beneath or to the west of the Hawaiian hotspot, with its root potentially spatially coincident with the Hawaiian mega-ULVZ

(Cottaar & Romanowicz, 2012). In addition, geodynamic modeling has suggested that upwelling flow at the edge and above LLVPs can explain plate motions over time and could be stable for hundreds of millions of years (Conrad et al., 2013). If ULVZ material is transported up all the way to the surface, it could then be the cause of anomalous isotopic signatures within the erupted magma, as suggested by for hotspots above mega-ULVZs based on geochemical evidence (e.g., Allegre et al., 1983; Mundl-Petermeier et al., 2020; Cottaar et al., 2022).

7 Summary

Detailed examination of exceptionally high-quality waveforms from an earthquake beneath the western Pacific Ocean, measured at stations of the USArray in North America, has revealed evidence for low velocity structures and seismic anisotropy at the base of the mantle near the eastern edge of the Pacific LLVP. We have suggested the presence of a thin layer at the base of the mantle beneath the central Pacific Ocean with a broad lateral extent showing reduced seismic velocities by $\sim$14 %. This provides additional support to the idea that such a layer could exist elsewhere in Earth, and may perhaps be ubiquitous, but it is not typically visible except in the case of extraordinarily high-quality and dense seismic data. Moreover, we have found evidence for two ULVZs at the edge of the Pacific LLVP, one of which has not been detected before and is located to the south of previously identified ULVZ structure. We have estimated the dimensions and velocity reductions of these ULVZs, which are likely connected to the complex low velocity structure at the base of the mantle in our study region, and may indicate variations in thickness and velocity of the broad and thin low velocity layer. Close to these ULVZs, potentially co-located with previously detected ULVZ structure, we infer the presence of lowermost mantle anisotropy, in a geometry that suggests $V_{SV} > V_{SH}$, from the splitting of $\mathrm{S_{diff}}$ waveforms of a particularly high-quality event. A geodynamic scenario compatible with our observation of $V_{SV} > V_{SH}$ is lattice-preferred orientation of anisotropic minerals, either located inside our outside the LLVP edge. Furthermore, shape-preferred orientation potentially caused by ULVZ material becoming entrained in upwelling mantle flow at the edge of the Pacific LLVP can explain our observations.

Data and software availability

All data used in this study are publicly available through IRIS (`http://service.iris.edu`), NCEDC (`http://service.ncedc.org`) and SCEDC (`http://service.scedc.caltech.edu`). We used data from USArray (IRIS Transportable Array, 2003) and data from networks AE (Arizona Geological Survey, 2007), AZ (UC San Diego, 1982), BK (Northern California Earthquake Data Center, 2014), CI (California Institute of Technology and United States Geological Survey Pasadena, 1926), CN (Natural Resources Canada (NRCAN Canada), 1975), G (Institut de physique du globe de Paris (IPGP) & École et Observatoire des Sciences de la Terre de Strasbourg (EOST), 1982), GS (Albuquerque Seismological Laboratory (ASL)/USGS, 1980), II (Scripps Institution of Oceanography, 1986), IU (Albuquerque Seismological Laboratory/USGS, 2014), IW (Albuquerque Seismological Laboratory (ASL)/USGS, 2003), LD (Lamont Doherty Earth Observatory (LDEO), Columbia University, 1970), NE (Albuquerque Seismological Laboratory (ASL)/USGS, 1994), PE (Penn State University, 2004), US (Albuquerque Seismological Laboratory (ASL)/USGS, 1990), and Z9 (Fischer et al., 2010). The synthetic seismograms for this study were computed using AxiSEM3D, which is publicly available at `https://github.com/AxiSEMunity` (Leng et al., 2016, 2019).

Acknowledgments

This work was funded by Yale University and by the U.S. National Science Foundation via grant No. EAR-2026917 to MDL. We thank Ed Garnero, Dan Frost, Shun Karato, Regina Maass and the Yale seismology group for helpful discussions. We are grateful to Jenny Jenkins for providing the plotting code for Figure 8 from Jenkins et al. (2021). We thank the Yale Center for Research Computing for providing the necessary research computing infrastructure for this study, and Tom Langford for optimizing AxiSEM3D on the Grace cluster. The Generic Mapping Tools (Wessel & Smith, 1998), ObsPy (Beyreuther et al., 2010), SplitRacer (Reiss & Rümpker, 2017), and AxiSEM3D (Leng et al., 2016, 2019) were used in this research. We are grateful to Jenny Jenkins, Yvonne Fröhlich and Joachim Ritter for their very constructive comments that helped us improve the manuscript.

Figures

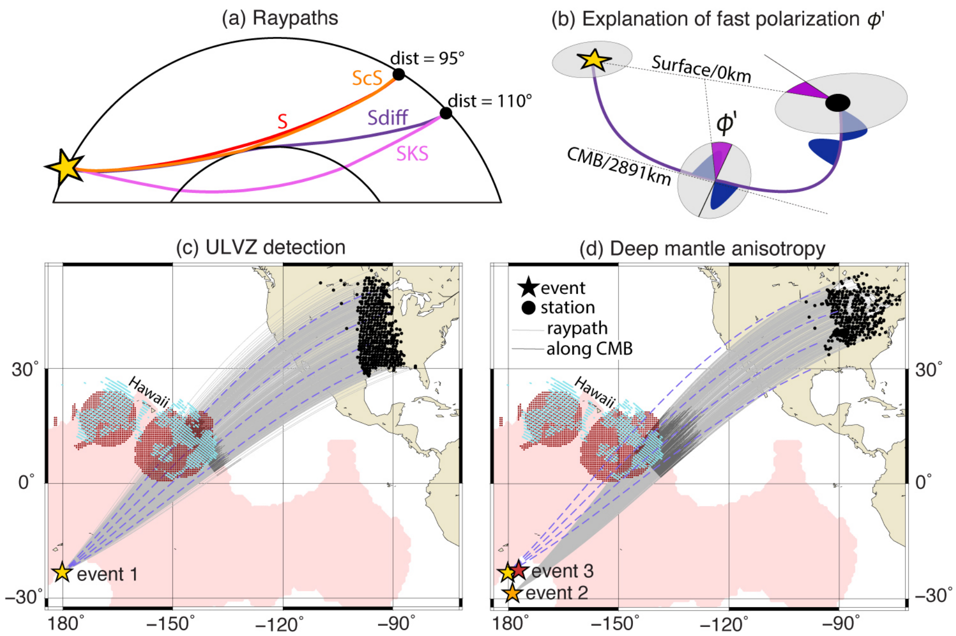

Figure 1. Source-receiver configuration used in this study. Sources are shown as colored stars and receivers as black circles. (a) Schematic cross-section showing the S (red line) and ScS (orange line) raypaths for an epicentral distance of 95° as well as the S_{diff} (violet line) and SKS (pink line) raypaths for a distance of 110°. (b) Explanation of the fast polarization direction ϕ' (similar to Nowacki et al. (2010)), projected to the lowermost mantle (purple angle). The quasi S wave, aligned with the fast polarization direction, is shown in blue color. Vertical fast polarization directions are indicated by $\phi \approx 0°$ and horizontal fast polarization directions by $\phi \approx 90°$. (c) Source-receiver setup for ULVZ detection. Raypaths for event 1 (yellow star) are shown as gray lines (dark gray where S_{diff} travels along the CMB, and light gray otherwise). Blue dashed lines indicate azimuths in 5° steps, starting from 45° for the northernmost line. The Pacific LLVP in 2700 km depth (as agreed by 3 out of 5 models in a cluster analysis by Cottaar and Lekic (2016)) is shown in pink. Red dots show locations and extent of previously suggested ULVZs in or close to our study region, compiled by Yu and Garnero (2018). We also added the ULVZs from Lai et al. (2022) and Sun et al. (2019) to this selection. Turquoise color shows those regions for which Jenkins et al. (2021) inferred shear velocity reductions > 5% assuming an ULVZ thickness of 10 km. (d) Same plotting conventions as in panel (a) for event 2 (orange), which is used for the detection of lowermost mantle anisotropy. The location of event 3 is indicated by a red star.

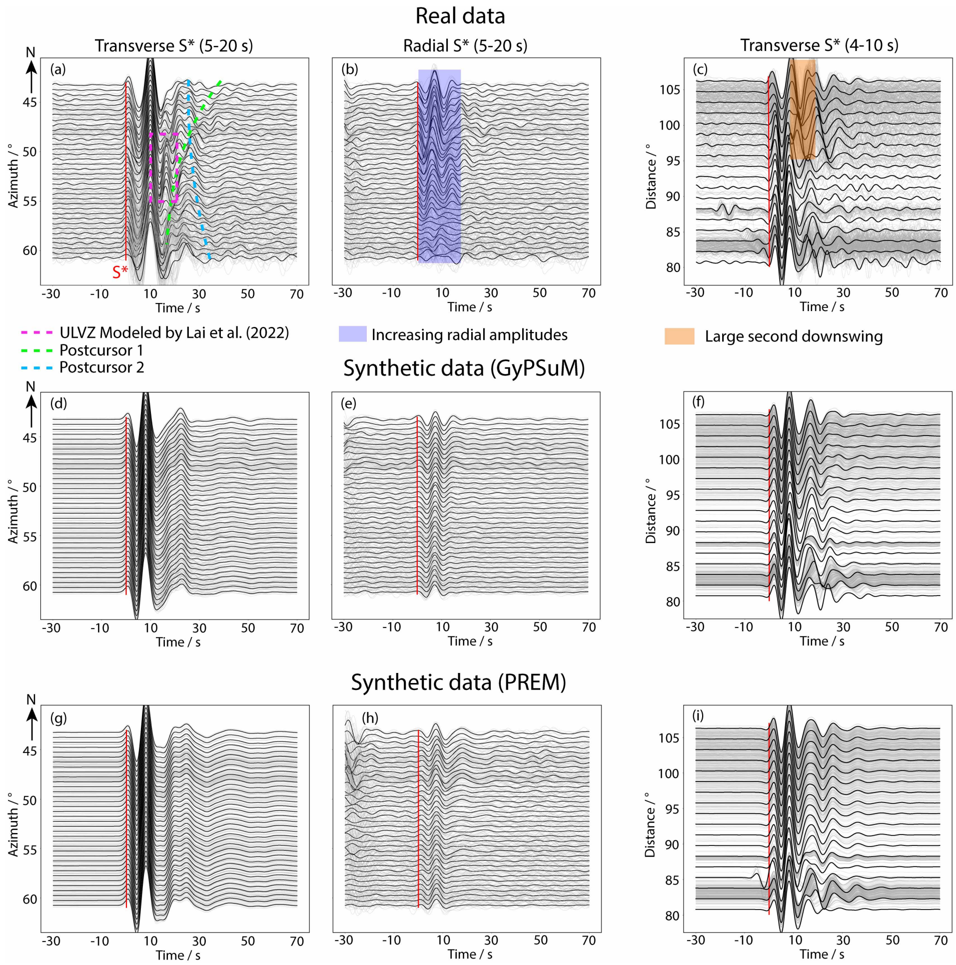

Figure 2. Real (a-c) and synthetic (d-i) velocity seismograms for event 1, stacked as a function of azimuth (a,b,d,e,g,h) and distance (c,f,g), after alignment to the minimum transverse amplitudes. Individual waveforms are shown as gray lines and stacks as black lines. Approximate S^* arrivals are shown by vertical red lines. (a) Transverse component seismograms with three different postcursors (see legend), bandpass-filtered between 5 and 20 s. One postcursor was modelled as ULVZ structure by Lai et al. (2022), while postcursors 1 and 2 indicate potentially unknown ULVZ structure. (b) Radial components, processed like the transverse components in (a). Radial component amplitudes (blue shading) increase for more northerly azimuths (c) Transverse component seismograms displayed as a function of distance after bandpass-filtering retaining periods between 4 and 10 s. The large second downswing is marked by orange shading. (d-f) Same as (a-c) for GyPSuM (Simmons et al., 2010) synthetics with a PREM background model. (g-i) Same as (a-c) for PREM background model. Postcursors are not reproduced in the synthetic seismograms (a,d,g); neither is the distance dependent behavior of the real data (c,f,i). For event 1, an average of 36 traces contributes to each azimuth bin and an average of 52 traces to each distance bin.

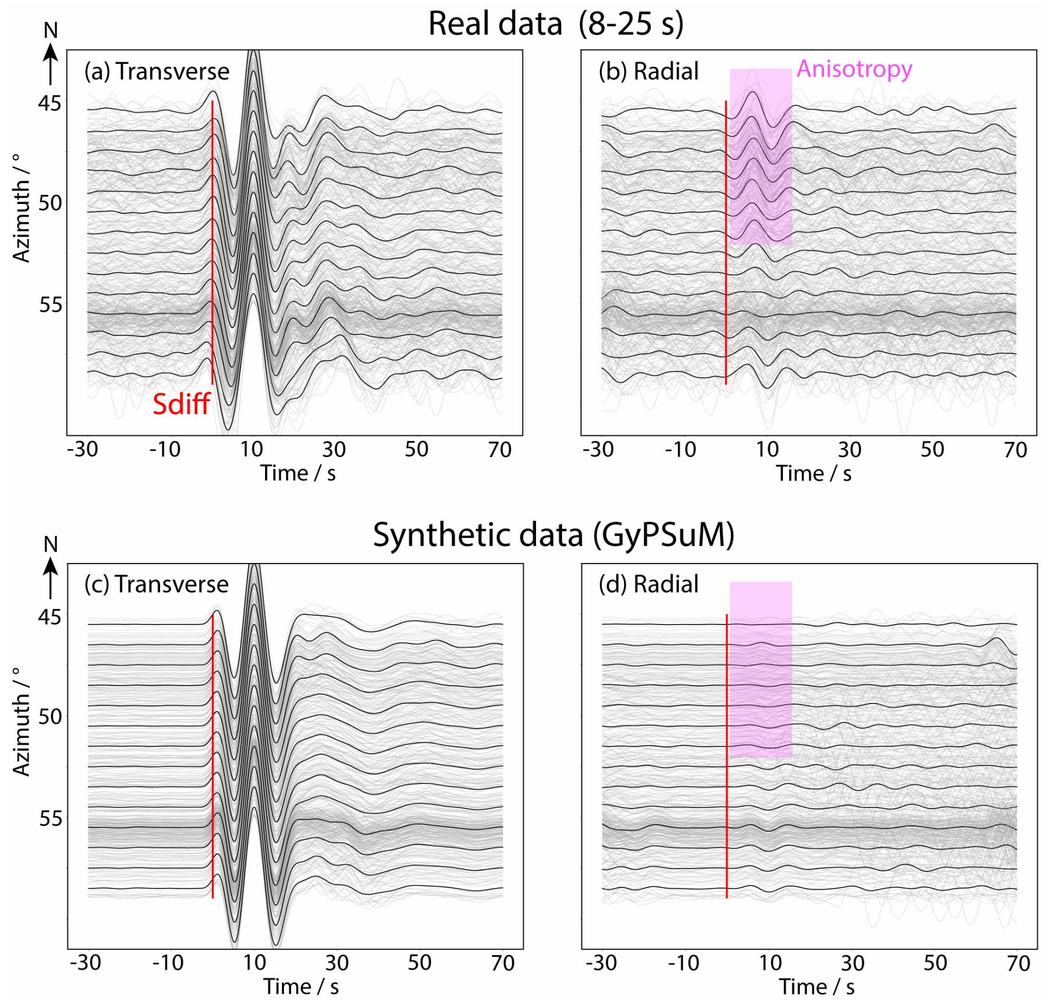

Figure 3. Real (a: transverse; b: radial) and synthetic (c: transverse; d: radial) velocity seismograms for event 2. Plotting conventions are similar to Figure 2. Red solid lines indicate the approximate S_{diff} arrival times. Synthetics were computed for GyPSuM synthetics with a PREM background model. Clearly discernible radial energy arrives on the radial components of the real data seismograms (b) while radial energy is almost absent between azimuths 45° and 53° (pink shading) for the synthetic seismograms (d). For event 2, an average of 28 traces contribute to each azimuth bin.

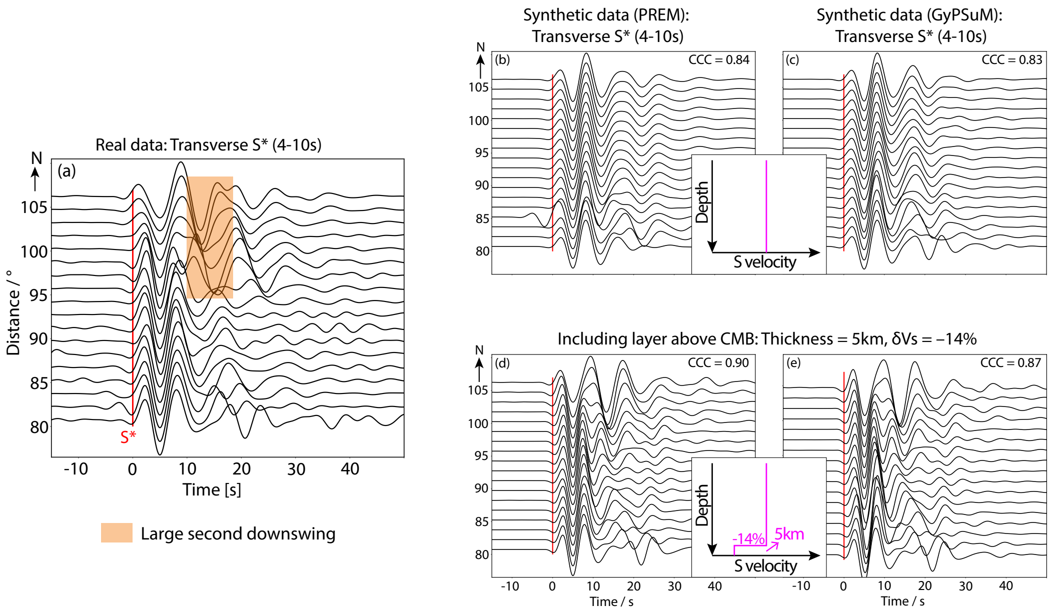

Figure 4. Real (a) and synthetic (b-e) transverse component velocity seismograms for event 1, displayed as function of distance. Plotting conventions for each panel are the same as in Figure 2c, except that single station seismograms are not shown. Synthetic data are shown for PREM (b,d) and GyPSuM input models (c,e) without (b,c) and with (d,e) the inclusion of a 5 km thick layer with velocity reductions of 14 % compared to PREM (see insets). Cross-correlation coefficients (CCC) are noted in the upper right corner.

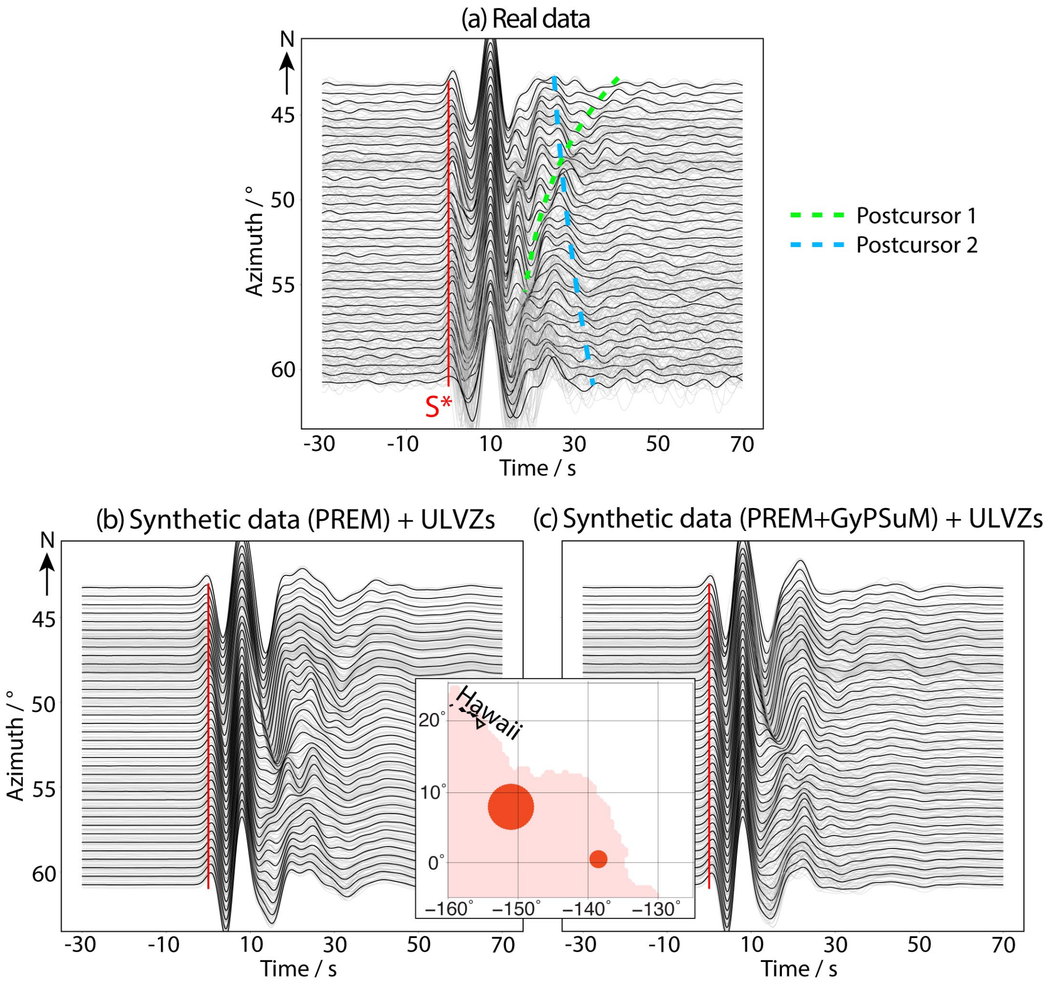

Figure 5. Real (a) and synthetic (b,c) transverse velocity seismograms for event 1, including both ULVZs (see inset). Plotting conventions for each subfigure are the same as in Figure 2a. Postcursors are only marked by dashed lines in panel a. (b) Synthetic seismograms for isotropic PREM as background model. (c) Same as (b) for PREM+GyPSuM. Inset: Geographical locations of modeled ULVZs (red circles). Pink colors mark the extent of the Pacific LLVP.

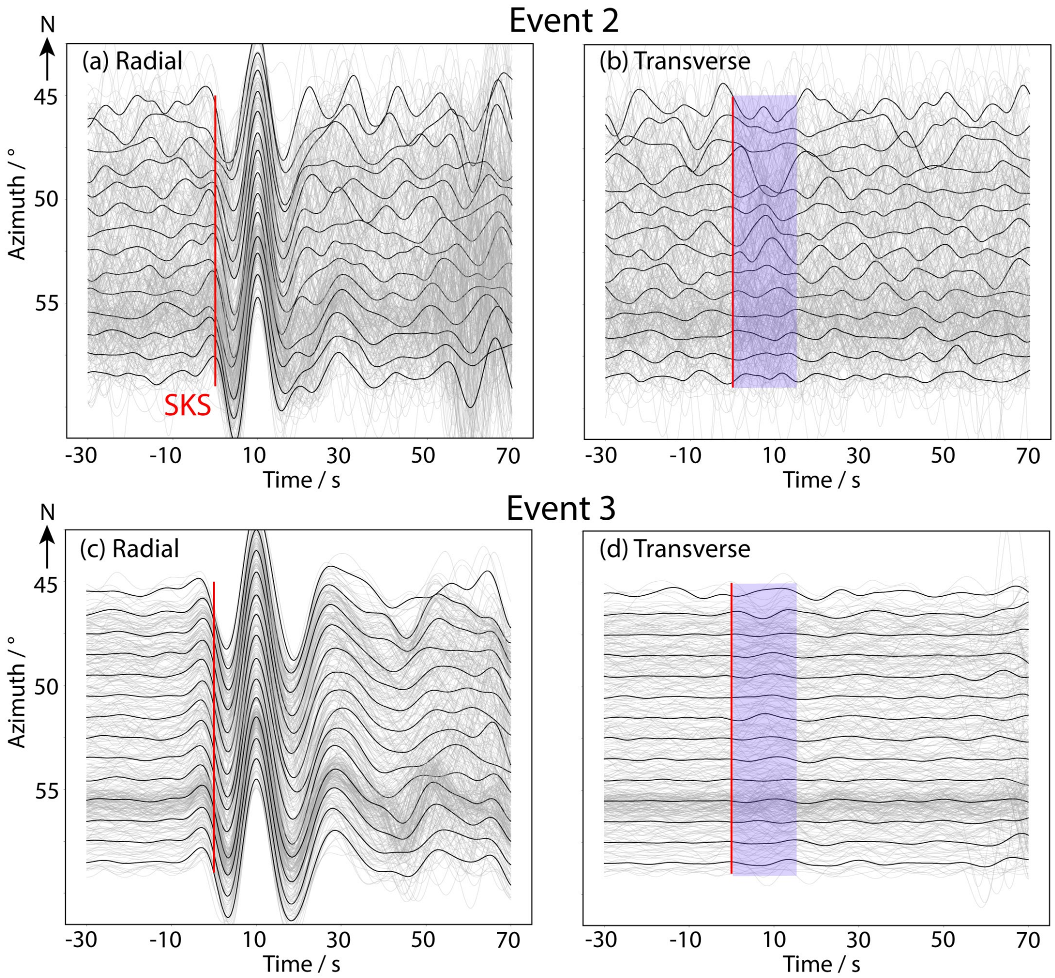

Figure 6. Radial (a,c) and transverse (b,d) SKS velocity seismograms as a function of azimuth for events 2 (a,b) and 3 (c,d). Plotting conventions for each panel are similar to Figure 2a. Red solid lines indicate the approximate SKS arrival times, and blue shading marks arriving SKS transverse component energy. For events 2 and 3, an average of 28 traces contribute to each azimuth bin.

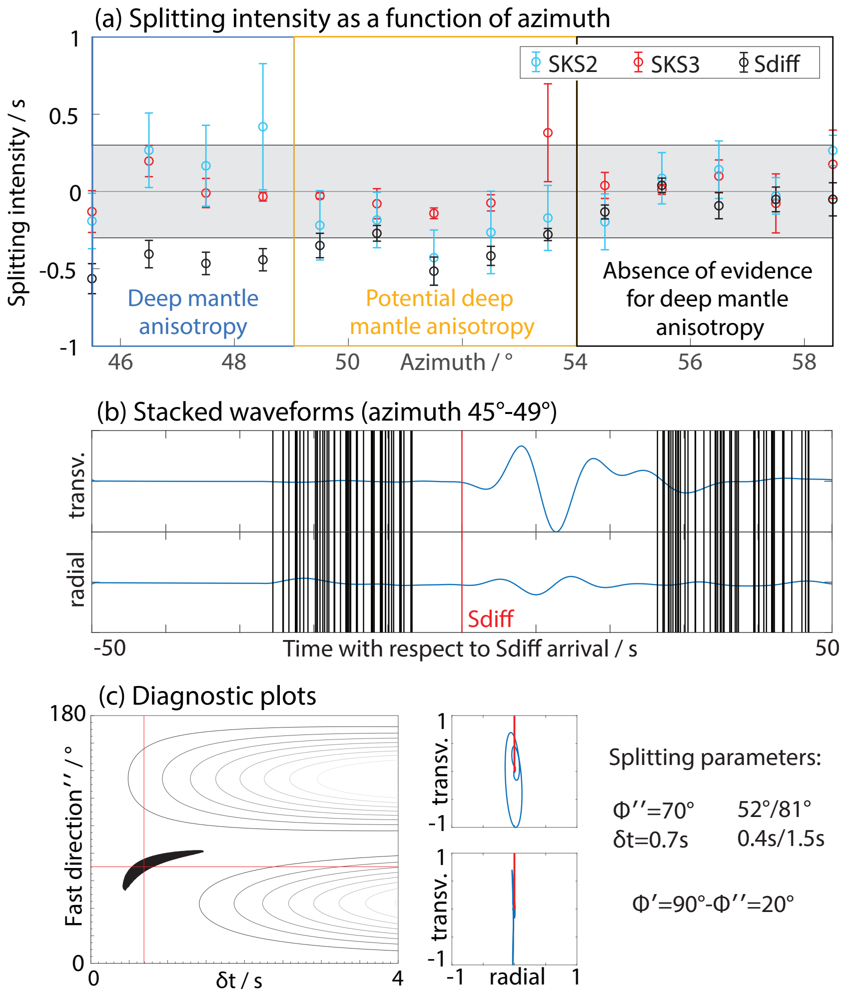

Figure 7. Splitting results for the investigations of lowermost mantle anisotropy. (a) Splitting intensities as a function of azimuth for 1° azimuth stacks. Values for S_{diff} are shown in black and for SKS in blue (event 2) and red (event 3). The gray shaded area indicates splitting intensities with lower absolute values than 0.3, which is practically indistinguishable from null splitting. Error bars indicate 95% confidence intervals. SKS and S_{diff} are split differentially in the azimuth range 45° to 49° (indicating deep mantle anisotropy), potentially differentially split between 49° to 54° azimuth (potentially indicating deep mantle anisotropy) and only weakly split elsewhere (no evidence for deep mantle anisotropy). (b) Stacked velocity waveforms for azimuths 45° to 49°. The approximate S_{diff} arrival is indicated by a solid red line. The start and end of 50 randomly selected time windows used for the splitting analysis are indicated by black lines. (c) Left: The best fitting splitting parameters are shown in the $\phi'' - \delta t$-plane, with black color indicating the 95% confidence region, and the red cross indicating the best-fitting combination of values. Right: The upper diagram shows the particle motion for the stack, the lower diagrams for the waveforms that were corrected for splitting. The red lines in the diagrams indicate the backazimuthal direction.

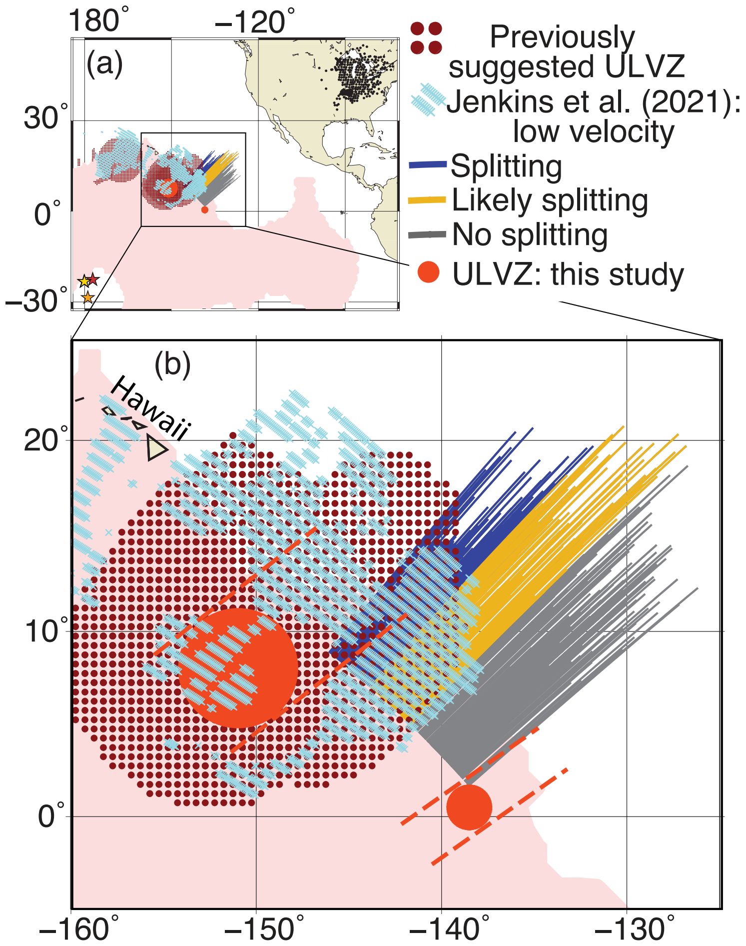

Figure 8. Summary map of ULVZ and anisotropy findings with similar plotting conventions as in Figure 1. (a) Events used in this study are shown as colored stars and stations as black circles. The Pacific LLVP is shown in pink, dark blue dots indicate the extent of previously suggested ULVZ structure (Yu & Garnero, 2018; Sun et al., 2019; Lai et al., 2022) and turquoise color shows those regions for which Jenkins et al. (2021) inferred shear velocity reductions $> 5\%$ assuming a ULVZ thickness of 10 km (see legend). The ULVZs found in this study are plotted as solid light red circles, with their location uncertainty indicated by dashed lines (as discussed in Section 6.1). Raypath lengths of S_{diff} along the CMB are shown in different colors, depending on whether shear-wave splitting due to deep mantle anisotropy has been detected (see legend). (b) Zoom-in to the study region using the same plotting conventions as in (a).

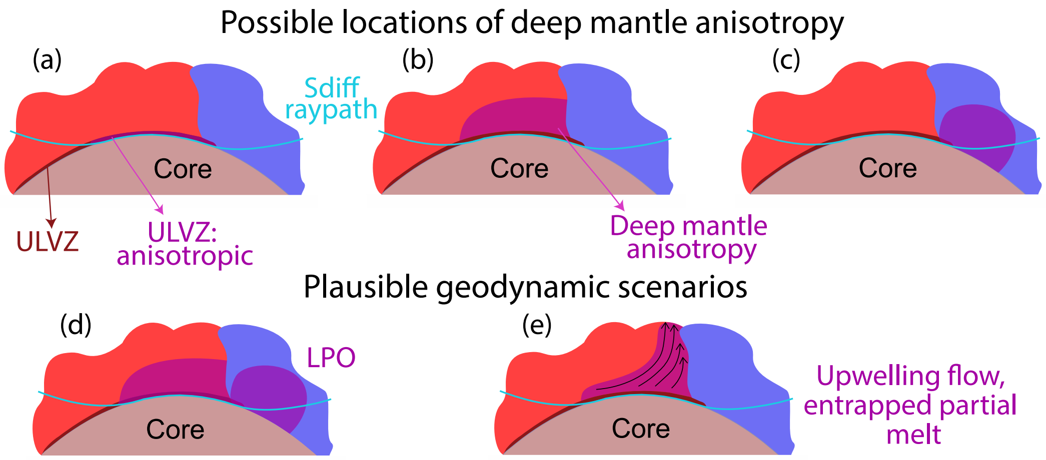

Figure 9. Possible locations of deep mantle anisotropy (a-c) and geodynamic scenarios consistent with deep mantle anisotropy observations (d-e). LLVP structure is schematically visualized by red color, structure outside the LLVP by blue color and ULVZs by dark red color. The S_{diff} raypath through the lowermost mantle is displayed as a light blue line, and seismic anisotropy is indicated by pink color. S_{diff} samples deep mantle anisotropy either (a) within the ULVZ structure, (b) within the LLVP and/or (c) outside of it. The measured splitting parameters (ϕ, δt) are consistent with (d) LPO at any of these three locations and (e) with upwelling flow at the LLVP edge, entrapping partial melt.

References

Albuquerque Seismological Laboratory (ASL)/USGS. (1980). *Us geological survey networks.* International Federation of Digital Seismograph Networks. Retrieved from `https://doi.org/10.7914/SN/GS`

Albuquerque Seismological Laboratory (ASL)/USGS. (1990). *United states national seismic network.* International Federation of Digital Seismograph Networks. Retrieved from `https://doi.org/10.7914/SN/US`

Albuquerque Seismological Laboratory (ASL)/USGS. (1994). *New england seismic network.* International Federation of Digital Seismograph Networks. Retrieved from `https://doi.org/10.7914/SN/NE`

Albuquerque Seismological Laboratory (ASL)/USGS. (2003). *Intermountain west seismic network.* International Federation of Digital Seismograph Networks. Retrieved from `https://doi.org/10.7914/SN/IW`

Albuquerque Seismological Laboratory/USGS. (2014). *Global seismograph network (gsn - iris/usgs).* International Federation of Digital Seismograph Networks. Retrieved from `https://doi.org/10.7914/SN/IU`

Allegre, C. J., Staudacher, T., Sarda, P., & Kurz, M. (1983). Constraints on evolution of Earth's mantle from rare gas systematics. *Nature*, *303*, 762–766. Retrieved from `https://doi.org/10.1038/303762a0`

Arizona Geological Survey. (2007). *Arizona broadband seismic network.* International Federation of Digital Seismograph Networks. Retrieved from `https://doi.org/10.7914/SN/AE`

Asplet, J., Wookey, J., & Kendall, M. (2020). A potential post-perovskite province in D$''$ beneath the Eastern Pacific: evidence from new analysis of discrepant SKS–SKKS shear-wave splitting. *Geophysical Journal International*, *221*, 2075–2090. Retrieved from `https://doi.org/10.1093/gji/ggaa114`

Asplet, J., Wookey, J., & Kendall, M. (2023). Inversion of shear wave waveforms reveal deformation in the lowermost mantle. *Geophysical Journal International*, *232*, 97–114. Retrieved from `https://doi.org/10.1093/gji/ggac328`

Avants, M., Lay, T., & Garnero, E. J. (2006). A new probe of ULVZ S-wave velocity structure: Array stacking of ScS waveforms. *Geophysical Research Letters*, *33*(7). Retrieved from `https://doi.org/10.1029/2005GL024989`

Beyreuther, M., Barsch, R., Krischer, L., Megies, T., Behr, Y., & Wassermann, J.

(2010, 06). Obspy: A python toolbox for seismology. *Seismological Research Letters*, *81*, 530–533. Retrieved from https://doi.org/10.1111/10.1785/gssrl.81.3.530

Borgeaud, A. F., Konishi, K., Kawai, K., & Geller, R. J. (2016). Finite frequency effects on apparent S-wave splitting in the D″ layer: comparison between ray theory and full-wave synthetics. *Geophysical Journal International*, *207*, 12–28. Retrieved from https://doi.org/10.1093/gji/ggw254

Burke, K., Steinberger, B., Torsvik, T. H., & Smethurst, M. A. (2008). Plume Generation Zones at the margins of Large Low Shear Velocity Provinces on the core–mantle boundary. *Earth and Planetary Science Letters*, *265*, 49–60. Retrieved from https://doi.org/10.1016/j.epsl.2007.09.042

California Institute of Technology and United States Geological Survey Pasadena. (1926). *Southern california seismic network.* International Federation of Digital Seismograph Networks. Retrieved from https://doi.org/10.7914/SN/CI

Chevrot, S. (2000). Multichannel analysis of shear wave splitting. *Journal of Geophysical Research: Solid Earth*, *105*, 21579–21590. Retrieved from https://doi.org/10.1029/2000JB900199

Conrad, C., Steinberger, B., & Torsvik, T. (2013). Stability of active mantle upwelling revealed by net characteristics of plate tectonics. *Nature*, *498*, 479–482. Retrieved from https://doi.org/10.1038/nature12203

Cottaar, S., & Lekic, V. (2016). Morphology of seismically slow lower-mantle structures. *Geophysical Journal International*, *207*, 1122–1136. Retrieved from https://doi.org/10.1093/gji/ggw324

Cottaar, S., Martin, C., Li, Z., & Parai, R. (2022). The root to the Galápagos mantle plume on the core-mantle boundary . *Seismica*, *1*. Retrieved from https://doi.org/10.26443/seismica.v1i1.197

Cottaar, S., & Romanowicz, B. (2012). An unusually large ULVZ at the base of the mantle near Hawaii. *Earth and Planetary Science Letters*, *355-356*, 213–222. Retrieved from https://doi.org/10.1016/j.epsl.2012.09.005

Cottaar, S., & Romanowicz, B. (2013). Observations of changing anisotropy across the southern margin of the African LLSVP. *Geophysical Journal International*, *195*, 1184–1195. Retrieved from https://doi.org/10.1093/gji/ggt285

Creasy, N., Miyagi, L., & Long, M. D. (2020). A Library of Elastic Tensors for

Lowermost Mantle Seismic Anisotropy Studies and Comparison With Seismic Observations. *Geochemistry, Geophysics, Geosystems*, *21*, e2019GC008883. Retrieved from https://doi.org/10.1029/2019GC008883

Creasy, N., Pisconti, A., Long, M. D., & Thomas, C. (2021). Modeling of seismic anisotropy observations reveals plausible lowermost mantle flow directions beneath Siberia. *Geochemistry, Geophysics, Geosystems*, e2021GC009924. Retrieved from https://doi.org/10.1029/2021GC009924

Creasy, N., Pisconti, A., Long, M. D., Thomas, C., & Wookey, J. (2019). Constraining lowermost mantle anisotropy with body waves: a synthetic modelling study. *Geophysical Journal International*, *217*(2), 766-783. Retrieved from https://doi.org/10.1093/gji/ggz049

Dannberg, J., Myhill, R., Gassmöller, R., & Cottaar, S. (2021). The morphology, evolution and seismic visibility of partial melt at the core–mantle boundary: implications for ULVZs. *Geophysical Journal International*, *227*, 1028–1059. Retrieved from https://doi.org/10.1093/gji/ggab242

Davaille, A., & Romanowicz, B. (2020). Deflating the LLSVPs: Bundles of Mantle Thermochemical Plumes Rather Than Thick Stagnant "Piles". *Tectonics*, *39*(10). Retrieved from https://doi.org/10.1029/2020TC006265

Davies, D. R., Goes, S., & Lau, H. (2015). Thermally dominated deep mantle LLSVPs: A review. *The Earth's Heterogeneous Mantle: A Geophysical, Geodynamical, and Geochemical Perspective*, 441–477. Retrieved from https://doi.org/10.1007/978-3-319-15627-9_14

Deng, J., Long, M. D., Creasy, N., Wagner, L., Beck, S., Zandt, G., … Minaya, E. (2017). Lowermost mantle anisotropy near the eastern edge of the Pacific LLSVP: constraints from SKS-SKKS splitting intensity measurements. *Geophysical Journal International*, *210*, 774–786. Retrieved from https://doi.org/10.1093/gji/ggx190

Dziewonski, A. M., & Anderson, D. L. (1981). Preliminary reference Earth model. *Physics of the Earth and Planetary Interiors*, *25*, 297–356. Retrieved from https://doi.org/10.1016/0031-9201(81)90046-7

Dziewonski, A. M., Lekic, V., & Romanowicz, B. A. (2010). Mantle anchor structure: An argument for bottom up tectonics. *Earth and Planetary Science Letters*, *299*, 69–79. Retrieved from https://doi.org/10.1016/j.epsl.2010.08

.013

Ekström, G., Nettles, M., & Dziewoński, A. (2012). The global CMT project 2004–2010: Centroid-moment tensors for 13,017 earthquakes. *Physics of the Earth and Planetary Interiors*, 1–9. Retrieved from https://doi.org/10.1016/j.pepi.2012.04.002

Ferrick, A. L., & Korenaga, J. (2023). Defining Earth's elusive thermal budget in the presence of a hidden reservoir. *Earth and Planetary Science Letters*, *601*, 117893. Retrieved from https://doi.org/10.1016/j.epsl.2022.117893

Finkelstein, G. J., Jackson, J. M., Said, A., Alatas, A., Leu, B. M., Sturhahn, W., & Toellner, T. S. (2018). Strongly Anisotropic Magnesiowüstite in Earth's Lower Mantle. *Journal of Geophysical Research: Solid Earth*, *123*(6), 4740–4750. Retrieved from https://doi.org/10.1029/2017JB015349

Foley, B. J., & Long, M. D. (2011). Upper and mid–mantle anisotropy beneath the Tonga slab. *Geophysical Research Letters*, *38*. Retrieved from https://doi.org/10.1029/2010GL046021

Ford, H. A., Long, M. D., He, X., & Lynner, C. (2015). Lowermost mantle flow at the eastern edge of the African Large Low Shear Velocity Province. *Earth and Planetary Science Letters*, *420*, 12–22. Retrieved from https://doi.org/10.1016/j.epsl.2015.03.029

French, S. W., & Romanowicz, B. A. (2014). Whole-mantle radially anisotropic shear velocity structure from spectral-element waveform tomography. *Geophysical Journal International*, *199*(3), 1303–1327. Retrieved from https://doi.org/10.1093/gji/ggu334

Hassan, R., Müller, D., Gurnis, M., Williams, S., & Flament, N. (2016). A rapid burst in hotspot motion through the interaction of tectonics and deep mantle flow. *Nature*, *533*, 239–242. Retrieved from https://doi.org/10.1038/nature17422

Hernlund, J., & Jellinek, M. (2010). Dynamics and structure of a stirred partially molten ultralow-velocity zone. *Earth and Planetary Science Letters*, *296*, 1–8. Retrieved from https://doi.org/10.1016/j.epsl.2010.04.027

Hernlund, J., Thomas, C., & Tackley, P. (2005). A doubling of the post-perovskite phase boundary and structure of the Earth's lowermost mantle. *Nature*, *434*, 882–886. Retrieved from https://doi.org/10.1016/10.1038/nature03472

Hernlund, J. W., & Bonati, I. (2019). Modeling Ultralow Velocity Zones as a Thin Chemically Distinct Dense Layer at the Core-Mantle Boundary. *Journal of Geophysical Research: Solid Earth*, *124*, 7902-7917. Retrieved from `https://doi.org/10.1029/2018JB017218`

Hosseini, K., Sigloch, K., Tsekhmistrenko, M., Zaheri, A., Nissen-Meyer, T., & Igel, H. (2019). Global mantle structure from multifrequency tomography using P, PP and P-diffracted waves. *Geophysical Journal International*, *220*(1), 96–141. Retrieved from `https://doi.org/10.1093/gji/ggz394`

Hutko, A. R., Lay, T., & Revenaugh, J. (2009). Localized double-array stacking analysis of pcp: D″ and ulvz structure beneath the cocos plate, mexico, central pacific, and north pacific. *Physics of the Earth and Planetary Interiors*, *173*(1), 60-74. Retrieved from `https://doi.org/10.1016/j.pepi.2008.11.003`

Institut de physique du globe de Paris (IPGP), & École et Observatoire des Sciences de la Terre de Strasbourg (EOST). (1982). *Geoscope, french global network of broad band seismic stations.* Institut de physique du globe de Paris (IPGP), Université de Paris. Retrieved from `https://doi.org/10.18715/GEOSCOPE.G`

IRIS Transportable Array. (2003). *USArray Transportable Array.* International Federation of Digital Seismograph Networks. Retrieved from `https://www.fdsn.org/networks/detail/TA/` doi: 10.7914/SN/TA

Jenkins, J., Mousavi, S., Li, Z., & Cottaar, S. (2021). A high-resolution map of Hawaiian ULVZ morphology from ScS phases. *Earth and Planetary Science Letters*, *563*, 116885. Retrieved from `https://doi.org/10.1016/j.epsl.2021.116885`

Kawai, K., & Geller, R. J. (2010). Waveform inversion for localized seismic structure and an application to D″ structure beneath the Pacific. *Journal of Geophysical Research: Solid Earth*, *115*. Retrieved from `https://doi.org/10.1029/2009JB006503`

Kawai, K., & Tsuchiya, T. (2009). Temperature profile in the lowermost mantle from seismological and mineral physics joint modeling. *Proceedings of the National Academy of Sciences*, *106*(52), 22119–22123. Retrieved from `https://doi.org/10.1073/pnas.0905920106`

Kendall, J.-M., & Silver, P. (1998). Investigating causes of "D" anisotropy, in The Core-Mantle Boundary Region. *Core–mantle boundary region*, *Geodynamic Series 28*, 97–118.

Kim, D., Lekić, V., Ménard, B., Baron, D., & Taghizadeh-Popp, M. (2020). Sequencing seismograms: A panoptic view of scattering in the core-mantle boundary region. *Science*, *368*(6496), 1223–1228. Retrieved from https://doi.org/10.1126/science.aba8972

Koelemeijer, P., Deuss, A., & Ritsema, J. (2017). Density structure of Earth's lowermost mantle from Stoneley mode splitting observations. *Nature Communications*, *8*. Retrieved from https://doi.org/10.1038/ncomms15241

Komatitsch, D., Vinnik, L. P., & Chevrot, S. (2010). SHdiff-SVdiff splitting in an isotropic Earth. *Journal of Geophysical Research: Solid Earth*, *115*(B7). Retrieved from https://doi.org/10.1029/2009JB006795

Labrosse, S., Hernlund, J., & Coltice, N. (2008). A crystallizing dense magma ocean at the base of the Earth's mantle. *Nature*, *450*, 866-869. doi: https://doi.org/10.1038/nature06355

Lai, V. H., Helmberger, D. V., Dobrosavljevic, V. V., Wu, W., Sun, D., Jackson, J. M., & Gurnis, M. (2022). Strong ULVZ and Slab Interaction at the Northeastern Edge of the Pacific LLSVP Favors Plume Generation. *Geochemistry, Geophysics, Geosystems*, *23*, e2021GC010020. Retrieved from https://doi.org/10.1029/2021GC010020

Lamont Doherty Earth Observatory (LDEO), Columbia University. (1970). *Lamont-doherty cooperative seismographic network.* International Federation of Digital Seismograph Networks. Retrieved from https://doi.org/10.7914/SN/LD

Lay, T., Garnero, E., & Williams, Q. (2004). Partial Melting in a Thermo-Chemical Boundary Layer at the Base of the Mantle. *Physics of the Earth and Planetary Interiors*, *146*, 441–467. Retrieved from https://doi.org/10.1016/j.pepi.2004.04.004

Lay, T., Hernlund, J., Garnero, E., & Thorne, M. (2006). A Post-Perovskite Lens and D″ Heat Flux Beneath the Central Pacific. *Science*, *314*, 1272-6. Retrieved from https://doi.org/10.1126/science.1133280

Leng, K., Nissen-Meyer, T., & van Driel, M. (2016). Efficient global wave propagation adapted to 3-D structural complexity: a pseudospectral/spectral-element approach. *Geophysical Journal International*, *207*(3), 1700-1721. Retrieved from https://doi.org/10.1093/gji/ggw363

Leng, K., Nissen-Meyer, T., van Driel, M., Hosseini, K., & Al-Attar, D. (2019). AxiSEM3D: broad-band seismic wavefields in 3-D global earth models with undulating discontinuities. *Geophysical Journal International*, *217*(3), 2125-2146. Retrieved from https://doi.org/10.1093/gji/ggz092

Lesher, C. E., Dannberg, J., Barfod, G. H., Bennett, N. R., Glessner, J. J. G., Lacks, D. J., & Brenan, J. M. (2020). Iron isotope fractionation at the core-mantle boundary by thermodiffusion. *Nature Geoscience*. Retrieved from https://doi.org/10.1038/s41561-020-0560-y

Li, M., McNamara, A., Garnero, E., & Yu, S. (2017). Compositionally-distinct ultra-low velocity zones on Earth's core-mantle boundary. *Nature Communications*, *177*. Retrieved from https://doi.org/10.1038/s41467-017-00219-x

Li, M., & Zhong, S. (2017). The source location of mantle plumes from 3D spherical models of mantle convection. *Earth and Planetary Science Letters*, *478*, 47–57. Retrieved from https://doi.org/10.1016/j.epsl.2017.08.033

Li, Z., Leng, K., Jenkins, J., & Cottaar, S. (2022). Kilometer-scale structure on the core–mantle boundary near Hawaii. *Nature Communications*, 1–8. Retrieved from https://doi.org/10.1038/s41467-022-30502-5

Long, M. D., & Becker, T. (2010). Mantle dynamics and seismic anisotropy. *Earth and Planetary Science Letters*, *297*, 341–354. Retrieved from https://doi.org/10.1016/j.epsl.2010.06.036

Long, M. D., & Silver, P. G. (2009). Shear Wave Splitting and Mantle Anisotropy: Measurements, Interpretations, and New Directions. *Surveys in Geophysics*, *30*, 407–461. Retrieved from https://doi.org/10.1007/s10712-009-9075-1

Lynner, C., & Long, M. D. (2014). Lowermost mantle anisotropy and deformation along the boundary of the African LLSVP. *Geophysical Research Letters*, 3447–3454. Retrieved from https://doi.org/10.1002/2014GL059875

Lynner, C., & Long, M. D. (2015). Heterogeneous seismic anisotropy in the transition zone and uppermost lower mantle: evidence from South America, Izu-Bonin and Japan. *Geophysical Journal International*, *201*, 1545–1552. Retrieved from https://doi.org/10.1093/gji/ggv099

McNamara, A. K., Garnero, E. J., & Rost, S. (2010). Tracking deep mantle reservoirs with ultra-low velocity zones. *Earth and Planetary Science Letters*, *299*, 1–9. Retrieved from https://doi.org/10.1016/j.epsl.2010.07.042

Mori, J., & Helmberger, D. V. (1995). Localized boundary layer below the mid-Pacific velocity anomaly identified from a PcP precursor. *Journal of Geophysical Research: Solid Earth*, *100*, 20359-20365. Retrieved from https://doi.org/10.1029/95JB02243

Mundl-Petermeier, A., Walker, R., Fischer, R., Lekic, V., Jackson, M., & Kurz, M. (2020). Anomalous 182W in high 3He/4He ocean island basalts: Fingerprints of Earth's core? *Geochimica et Cosmochimica Acta*, *271*, 194–211. Retrieved from https://doi.org/10.1016/j.gca.2019.12.020

Murakami, M., Hirose, K., Kawamura, K., Sata, N., & Ohishi, Y. (2004). Post-Perovskite Phase Transition in MgSiO3. *Science*, *304*, 855–858. Retrieved from https://doi.org/10.1126/science.1095932

Natural Resources Canada (NRCAN Canada). (1975). *Canadian national seismograph network.* International Federation of Digital Seismograph Networks. Retrieved from https://doi.org/10.7914/SN/CN

Northern California Earthquake Data Center. (2014). *Berkeley digital seismic network (bdsn).* Northern California Earthquake Data Center. Retrieved from https://doi.org/10.7932/BDSN

Nowacki, A., & Cottaar, S. (2021). Toward imaging flow at the base of the mantle with seismic, mineral physics, and geodynamic constraints. In *Mantle convection and surface expressions* (pp. 329–352). American Geophysical Union (AGU). Retrieved from https://doi.org/10.1002/9781119528609.ch13

Nowacki, A., Wookey, J., & Kendall, J.-M. (2010). Deformation of the lowermost mantle from seismic anisotropy. *Nature*, *467*, 1091–1094. Retrieved from https://doi.org/10.1038/nature09507

Nowacki, A., Wookey, J., & Kendall, J.-M. (2011). New advances in using seismic anisotropy, mineral physics and geodynamics to understand deformation in the lowermost mantle. *Journal of Geodynamics*, *52*, 205–228. Retrieved from https://doi.org/10.1016/j.jog.2011.04.003

Otsuka, K., & Karato, S.-i. (2012). Deep penetration of molten iron into the mantle caused by a morphological instability. *Nature*, *492*, 243–246. Retrieved from https://doi.org/10.1038/nature11663

Pachhai, S., Li, M., Thorne, M., Dettmer, J., & Tkalčić, H. (2022). Internal structure of ultralow-velocity zones consistent with origin from a basal magma ocean. *Nature Geoscience*, *15*. Retrieved from https://doi.org/0.1038/s41561-021-00871-5

Panning, M., & Romanowicz, B. (2006). A three-dimensional radially anisotropic model of shear velocity in the whole mantle. *Geophysical Journal International*, *167*, 361–379. Retrieved from https://doi.org/10.1111/j.1365-246X.2006.03100.x

Parisi, L., Ferreira, A. M. G., & Ritsema, J. (2018). Apparent Splitting of S Waves Propagating Through an Isotropic Lowermost Mantle. *Journal of Geophysical Research: Solid Earth*, *123*, 3909–3922. Retrieved from https://doi.org/10.1002/2017JB014394

Penn State University. (2004). *Pennsylvania state seismic network.* International Federation of Digital Seismograph Networks. Retrieved from https://doi.org/10.7914/SN/PE

Pisconti, A., Creasy, N., Wookey, J., Long, M. D., & Thomas, C. (2023). Mineralogy, fabric and deformation domains in D″ across the southwestern border of the African LLSVP. *Geophysical Journal International*, *232*(1), 705-724. Retrieved from https://doi.org/10.1093/gji/ggac359

Reiss, M., Long, M. D., & Creasy, N. (2019). Lowermost Mantle Anisotropy Beneath Africa From Differential SKS-SKKS Shear-Wave Splitting. *Journal of Geophysical Research: Solid Earth*, *124*(8), 8540–8564. Retrieved from https://doi.org/10.1029/2018JB017160

Reiss, M., & Rümpker, G. (2017). SplitRacer: MATLAB Code and GUI for Semiautomated Analysis and Interpretation of Teleseismic Shear-Wave Splitting. *Seismological Research Letters*, *88*, 392 – 409. Retrieved from https://doi.org/10.1785/0220160191

Fischer, K. M., Robert B. Hawman, & Lara S. Wagner. (2010). *Southeastern suture of the appalachian margin experiment.* International Federation of Digital Seismograph Networks. Retrieved from https://doi.org/10.7914/SN/Z9_2010

Revenaugh, J., & Meyer, R. (1997). Seismic evidence of partial melt within a possibly ubiquitous low-velocity layer at the base of the mantle. *Science*, *277*(5326), 670-673. Retrieved from https://doi.org/10.1126/science.277.5326.670

Ritsema, J., Deuss, A., van Heijst, H. J., & Woodhouse, J. H. (2011). S40RTS: a degree-40 shear-velocity model for the mantle from new Rayleigh wave dispersion, teleseismic traveltime and normal-mode splitting function measurements. *Geophysical Journal International*, *184*(3), 1223–1236. Retrieved from https://doi.org/10.1111/j.1365-246X.2010.04884.x

Ritsema, J., Lay, T., Garnero, E., & Benz, H. (1998). Seismic anisotropy in the lowermost mantle beneath the pacific. *Geophysical Research Letters*, *25*, 1229–1232. Retrieved from https://doi.org/10.1029/98GL00913

Russell, S., Irving, J. C., & Cottaar, S. (2022). Seismic visibility of melt at the core-mantle boundary from PKKP diffracted waves. *Earth and Planetary Science Letters*, *595*, 117768. doi: https://doi.org/10.1016/j.epsl.2022.117768

Scripps Institution of Oceanography. (1986). *Global seismograph network - iris/ida.* International Federation of Digital Seismograph Networks. Retrieved from https://doi.org/10.7914/SN/II

Silver, P. G., & Chan, W. W. (1991). Shear wave splitting and subcontinental mantle deformation. *Journal of Geophysical Research: Solid Earth*, *96*, 16429–16454. Retrieved from https://doi.org/10.1029/91JB00899

Simmons, N. A., Forte, A. M., Boschi, L., & Grand, S. P. (2010). GyPSuM: A joint tomographic model of mantle density and seismic wave speeds. *Journal of Geophysical Research: Solid Earth*, *115*. Retrieved from https://doi.org/10.1029/2010JB007631

Steinberger, B., Conrad, C. P., Osei Tutu, A., & Hoggard, M. J. (2019). On the amplitude of dynamic topography at spherical harmonic degree two. *Tectonophysics*, *760*, 221–228. Retrieved from https://doi.org/10.1016/j.tecto.2017.11.032 (Linking Plate Tectonics and Volcanism to Deep Earth Dynamics – a tribute to Trond H. Torsvik)

Sun, D., Helmberger, D., Lai, V. H., Gurnis, M., Jackson, J. M., & Yang, H.-Y. (2019). Slab Control on the Northeastern Edge of the Mid-Pacific LLSVP Near Hawaii. *Geophysical Research Letters*, *46*(6), 3142–3152. Retrieved from https://doi.org/10.1029/2018GL081130

Torsvik, T. H., van der Voo, R., Doubrovine, P. V., Burke, K., Steinberger, B., Ashwal, L. D., ... Bull, A. L. (2014). Deep mantle structure as a reference frame for movements in and on the Earth. *Proceedings of the National Academy of Sciences*, *111*(24), 8735–8740. Retrieved from https://doi.org/10.1073/pnas.1318135111

Trampert, J., Deschamps, F., Resovsky, J., & Yuen, D. (2004). Probabilistic Tomography Maps Chemical Heterogeneities Throughout the Lower Mantle. *Science*, *306*, 853–856. Retrieved from https://doi.org/10.1126/science.1101996

UC San Diego. (1982). *Anza regional network.* International Federation of Digital Seismograph Networks. Retrieved from https://doi.org/10.7914/SN/AZ

Vinnik, L., Breger, L., & Romanowicz, B. (1998). Anisotropic structures at the base of the Earth's mantle. *Nature*, *393*, 564–567. doi: 10.1038/31208

Vinnik, L., Farra, V., & Romanowicz, B. (1989). Observational evidence for diffracted SV in the shadow of the Earth's core. *Geophysical Research Letters*, *16*, 519–522. Retrieved from https://doi.org/GL016i006p00519

Vinnik, L., Romanowicz, B., Le Stunff, Y., & Makeyeva, L. (1995). Seismic anisotropy in the D" layer. *Geophysical Research Letters*, *22*(13), 1657–1660. Retrieved from https://doi.org/10.1029/95GL01327

Walsh, E., Arnold, R., & Savage, M. K. (2013). Silver and Chan revisited. *Journal of Geophysical Research: Solid Earth*, *118*, 5500–5515. Retrieved from https://doi.org/10.1002/jgrb.50386

Wang, Y., & Wen, L. (2004). Mapping the geometry and geographic distribution of a very low velocity province at the base of the Earth's mantle. *Journal of Geophysical Research: Solid Earth*, *109*. Retrieved from https://doi.org/10.1029/2003JB002674

Wenk, H.-R., & Romanowicz, B. (2017). Anisotropy in the deep Earth. *Physics of the Earth and Planetary Interiors*, *269*, 58–90. Retrieved from https://doi.org/10.1016/j.pepi.2017.05.005

Wessel, P., & Smith, W. H. F. (1998). New, improved version of generic mapping tools released. *Eos, Transactions American Geophysical Union*, *79*, 579–579. Retrieved from https://doi.org/10.1029/98EO00426

Wolf, J., Creasy, N., Pisconti, A., Long, M. D., & Thomas, C. (2019). An investigation of seismic anisotropy in the lowermost mantle beneath Iceland. *Geophysical Journal International*, *219*(Supplement_1), S152 – S166. Retrieved from https://doi.org/10.1093/gji/ggz312

Wolf, J., & Evans, D. A. D. (2022). Reconciling supercontinent cycle models with ancient subduction zones. *Earth and Planetary Science Letters*, 117293. Retrieved from https://doi.org/10.1016/j.epsl.2021.117293

Wolf, J., Frost, D. A., Long, M. D., Garnero, E., Aderoju, A. O., Creasy, N., & Bozdağ, E. (2023). Observations of Mantle Seismic Anisotropy Using Array Techniques: Shear-Wave Splitting of Beamformed SmKS Phases. *Journal of Geophysical Research: Solid Earth*, *128*(1), e2022JB025556. Retrieved from https://doi.org/10.1029/2022JB025556

Wolf, J., & Long, M. D. (2022). Slab-driven flow at the base of the mantle beneath the northeastern Pacific Ocean. *Earth and Planetary Science Letters*, *594*, 117758. Retrieved from https://doi.org/10.1016/j.epsl.2022.117758

Wolf, J., Long, M. D., Creasy, N., & Garnero, E. (2023). On the measurement of Sdiff splitting caused by lowermost mantle anisotropy. *Geophysical Journal International*. Retrieved from https://doi.org/10.1093/gji/ggac490

Wolf, J., Long, M. D., Leng, K., & Nissen-Meyer, T. (2022a). Sensitivity of SK(K)S and ScS phases to heterogeneous anisotropy in the lowermost mantle from global wavefield simulations. *Geophysical Journal International*, 366 – 386. Retrieved from https://doi.org/10.1093/gji/ggab347

Wolf, J., Long, M. D., Leng, K., & Nissen-Meyer, T. (2022b). Constraining deep mantle anisotropy with shear wave splitting measurements: Challenges and new measurement strategies. *Geophysical Journal International*, 507 – 527. Retrieved from https://doi.org/10.1093/gji/ggac055

Wookey, J., Kendall, J.-M., & Rümpker, G. (2005b). Lowermost mantle anisotropy beneath the north Pacific from differential S-ScS splitting. *Geophysical Journal International*, *161*, 829–838. Retrieved from https://doi.org/10.1111/j.1365-246X.2005.02623.x

Yu, S., & Garnero, E. J. (2018). Ultralow Velocity Zone Locations: A Global Assessment. *Geochemistry, Geophysics, Geosystems*. Retrieved from https://doi.org/10.1002/2017GC007281

Yuan, K., & Romanowicz, B. (2017). Seismic evidence for partial melting at the root of major hot spot plumes. *Science*, *357*, 393-397. Retrieved from https://doi.org/10.1126/science.aan0760